Passivation and Localized Corrosion Resistance of Al0.3Cr0.5Fe2MoxNi1.5Ti0.3 Compositionally Complex Alloys: Effect of Mo Content

S.B. Inman, Junsoo Han, M.A. Wischhusen, J. Qi, S.R. Agnew, Kevin Ogle, J.R. Scully

▶ **To cite this version:**

S.B. Inman, Junsoo Han, M.A. Wischhusen, J. Qi, S.R. Agnew, et al.. Passivation and Localized Corrosion Resistance of Al0.3Cr0.5Fe2MoxNi1.5Ti0.3 Compositionally Complex Alloys: Effect of Mo Content. Corrosion Science, 2024, 227, pp.111692. 10.1016/j.corsci.2023.111692 . hal-04300127

HAL Id: hal-04300127
https://hal.science/hal-04300127

Submitted on 22 Nov 2023

HAL is a multi-disciplinary open access archive for the deposit and dissemination of scientific research documents, whether they are published or not. The documents may come from teaching and research institutions in France or abroad, or from public or private research centers.

L'archive ouverte pluridisciplinaire **HAL**, est destinée au dépôt et à la diffusion de documents scientifiques de niveau recherche, publiés ou non, émanant des établissements d'enseignement et de recherche français ou étrangers, des laboratoires publics ou privés.

Passivation and Localized Corrosion Resistance of $Al_{0.3}Cr_{0.5}Fe_2Mo_xNi_{1.5}Ti_{0.3}$ Compositionally Complex Alloys: Effect of Mo Content

S.B. Inman[1,2,+], J. Han[1,2,3,4], M.A. Wischhusen[1], J. Qi[5,6], S.R. Agnew[1], K. Ogle[4], J.R. Scully[1,2]

[1]Department of Materials Science and Engineering, University of Virginia, 395 McCormick Road, Charlottesville, VA 22904, USA

[2]Center for Electrochemical Science and Engineering, University of Virginia, 395 McCormick Road, Charlottesville, VA 22904, USA

[3]Sorbonne Université, CNRS, Laboratoire Interfaces et Systèmes Electrochimiques (LISE), F-75005, Paris, France

[4]Chimie ParisTech, PSL Research University, CNRS, Institut de Recherche Chimie Paris (IRCP), F-75005, Paris, France

[5]Department of Physics, University of Virginia, 382 McCormick Road, Charlottesville, VA 22904, USA

[6]Department of Materials Science and Engineering, Northwestern University, 2220 Campus Drive, Evanston, IL 60208, USA

[+]Corresponding author: sbi3dk@virginia.edu

Journal Pre-proof

Abstract

$Al_{0.3}Cr_{0.5}Fe_2Mo_xNi_{1.5}Ti_{0.3}$ (x = 0, 0.05, 0.15) FCC+$L2_1$ compositionally complex alloys are investigated using electrochemical and surface science methods in 0.1 M Na_2SO_4 and 0.1 M NaCl at pH 4 and 10. Mo is mainly found in the FCC phase and amplifies Al and Ti partitioning. The passive film is enriched in Cr(III), Ti(IV), Mo(IV)/Mo(VI), and (at pH 4) Al(III) with elemental fates tracked during film formation and dissolution. Mo presence does not enhance Cr or Ni passivation, instead promoting Ti(IV). Pitting and repassivation potentials increase at higher Mo concentrations, suggesting improved resistance to localized corrosion often initiated at FCC-$L2_1$ interfaces.

Keywords:

Passivation; Compositionally complex alloys; High entropy alloys; Molybdenum; Atomic emission spectroelectrochemistry; X-ray photoelectron spectroscopy

Introduction

Compositionally complex alloys (CCAs), alloys which contain four or more elements at concentrations above 5 at. %, can have a range of beneficial properties including mechanical strength and corrosion resistance [1-5]. Improved homogeneity of passivating elements is often suggested to limit localized solute depletion that may function as preferential sites for localized corrosion [2, 3].

Light-weight elements, particularly Al and Ti, can impart both corrosion resistance and reduced density when added to CCAs [1, 6]. In particular, passivity may be enhanced by simultaneous presence with Cr in the passive film [7, 8]. However, increased Al and/or Ti concentrations in face centered cubic (FCC) CCAs have been shown to lead to the formation of BCC [6, 9-15], B2 [11, 14, 16], and/or Heusler [6, 17-19] phases, where the second phase regions are enriched in Al, Ti, and often Ni [13, 14, 18, 20]. Interfaces created by such secondary phase formation have been suggested to function as initiation sites for localized corrosion, decreasing overall corrosion resistance despite the thermodynamic stability of Ti and Al oxides[1] [15, 18, 21]. Thus, phase stability issues limit Al and/or Ti concentration, necessitating further alloying additions to limit the effects of microstructural segregation-driven localized corrosion.

Mo has been long established as improving corrosion resistance, most commonly in stainless steels [22, 23]. Although there is no universal agreement for the mechanism behind the contribution of Mo to the corrosion resistance of stainless steels, it is generally accepted as effective in preventing localized corrosion mechanisms such as pitting. Newman suggested Mo, in its non-oxidized state, acts as a

[1] High temperature annealing treatments may limit localized solute depletion, however, two-phase equilibrium microstructures allow individual phases to be depleted of individual passivating elements, increasing the risk of localized corrosion.

Journal Pre-proof

corrosion inhibitor in stainless steels [24] while Hashimoto et al. proposed inhibition occurs via a Mo oxyhydroxide layer [25]. Alternatively, Mo has been suggested to be present in the passive films across multiple valences and species [23, 26, 27]. Mo has also been shown to improve repassivation ability and rates in stainless steels and Ni-Cr-Mo alloys [28, 29], potentially due to redeposition after dissolution [30]. Tranchida et al. suggested Mo slows transpassive dissolution rates by doping the Cr oxide film formed on stainless steels and altering the band gap to limit the formation of unstable Cr species [31].

Lutton et al. evaluated alloying Ni-Cr binary alloys with Mo, finding Mo to improve the corrosion resistance and increase the enrichment of Cr in the passive film in acidic and basic NaCl solutions [32]. The phenomena were attributed to a favorable Cr-Mo synergy promoting O adsorption and low concentrations of oxidized Mo acting as a doping agent in the passive film. Lloyd et al. suggested Mo addition to Ni-Cr alloys to be most significant at high potentials where Cr(VI) is stable, attributing the beneficial effects of Mo to limitations of Cr-induced transpassivity [33]. Additionally, Mo addition allows for stable oxide formation over grain facets at orientations for which it does not occur on Ni-Cr binaries of the same Cr content [34]. Such Ni-Cr-Mo alloys have been utilized to form a baseline survey of potential mechanisms for the beneficial contributions of Mo to the corrosion resistance of FCC steels and similar alloys [27, 35]. While Mo addition has been suggested to be beneficial for both Fe-Cr and Ni-Cr based alloys, similar effects are not suggested in Cr-free counterparts [23, 36, 37]. For this reason, Mo is considered to have synergetic behavior with Cr.

Alloying benefits of Mo have been shown to extend into CCA microstructures. For example, when alloyed to the Co-Cr-Fe-Ni system, Mo may enhance mechanical strength by acting as a solid solution strengthener [38]. Dai et al. evaluated varying annealing procedures to optimize the mechanical and corrosion resistance of $FeCoCrNiMo_{0.1}$ CCAs [39]. At high Mo concentrations, second phase strengthening is possible though second phase formation in FCC CCAs, in part due to the well-established ferritic stabilization of Mo in conventional Fe alloys. In the $AlCoCrFeNiMo_x$ system, higher Mo concentrations

Journal Pre-proof

increase strength by forming an eutectic structure with a second phase enriched in Cr, Fe, and Mo [40]. Mo frequently combines with Cr by forming σ or μ intermetallic phases [20, 40-46].

Mo, and its influence on second phase formation, has also been shown to affect the corrosion resistance of CCAs such as those in the Co-Cr-Fe-Mn-Ni system [7, 20, 37, 39, 41, 42, 45-47] pioneered by Cantor et al. [48]. Niu et al. showed increasing Mo content improved corrosion resistance in the $CoCrFeNiMo_x$ system in addition to improving mechanical strength due to the formation of σ and μ intermetallic phases ranging from nm to μm size scale. A Mo concentration of 11.1 at. % had the highest corrosion potential of all tested compositions and formed few stable pits [46]. Similarly, Wang et al. observed more positive pitting potentials in chloride environments with increased Mo concentration added to the $(CoCrFeNi)_{1-x}Mo_x$ system. However, more frequent pitting, higher current densities, and a more negative corrosion potential were observed with 3 wt. % Mo added due to the formation of a σ phase. Such decreases were not observed during polarization in sulfuric acid [20]. Unlike most cases, where σ phases are likely at higher Mo concentrations, Linder et al. observed σ phase only at low Mo concentrations in magnetron sputtered $CoCrFeMo_xNi$ thin films. Little effect was observed on room temperature corrosion behaviour in acidic sulfate solutions, however, corrosion resistance improved with Mo concentration at 80 ˚C. Additionally, increased surface cation fractions of both Cr and Mo were observed in the passive film of the CCAs with increasing Mo concentration [45].

Chou et al. evaluated the corrosion resistance of the $Co_{1.5}CrFeNi_{1.5}Ti_{0.5}Mo_x$ CCA system [41]. Increasing Mo concentrations marked a transition from single phase FCC to an FCC with σ phase dendritic microstructure. The corrosion resistance decreased with increased Mo concentration in both acidic (H_2SO_4) and basic (NaOH) solutions. In neutral NaCl solutions, the Mo-free CCA had a distinct pitting potential well below the potentials of similar current increases for all evaluated Mo containing CCAs, which dissolved in a transpassive manner following formation of a stable passive film. The breakdown behavior of the Mo-containing CCAs was identified by a negative hysteresis and verified by scanning

Journal Pre-proof

electron microscopy (SEM) imaging to indicate a lack of pitting. Improved resistance to general corrosion at lower Mo concentrations and to pitting corrosion at higher concentration suggests that the optimal Mo concentration for passivity and localized corrosion resistance may differ.

Similarly, Rodriguez et al. observed an increased breakdown potential and improved repassivation behavior with the addition of 7.64 at. % Mo to the $CoCrFeNi_2$ CCA [42]. Improved overall corrosion resistance was speculated to occur due to the formation of an improved protective layer at grain boundaries and other preferential sites for localized corrosion. Shang et al. evaluated the microstructure and corrosion resistance of a series of $CoCrFeMnNiMo_x$ CCAs [43]. Increased Mo concentration was suggested to improve the corrosion resistance. However, concentrations which were high enough to promote the formation of a σ phase were suggested to harm corrosion resistance. Mo was observed in the oxide film with X-ray photoelectron spectroscopy (XPS) surface analysis, suggesting it may play a role in the passivation process. The existing body of work highlights how balancing the beneficial pitting and passivity contributions with phase partitioning, intermetallic formation, cost, and density consequences adds considerable complexity to optimization of Mo concentration in CCAs.

Although Mo has well established benefits to corrosion resistance within traditional binary alloys as well as the CCA field, the addition to Al and Ti-containing CCAs is notably less explored. Mo has been shown to improve corrosion resistance in the Al-Ti-Mo system, although it also promoted chemical segregation leading to microgalvanic corrosion [49]. Limited work has suggested increased Mo concentrations in Al and Ti containing CCAs with modest Cr concentrations also promote the formation of separate phases [40, 41]. Furthermore, the increase in alloy density from Mo additions runs contrary to the light-weight applications for which Al and Ti CCAs are often targeted [6]. Despite potential adverse effects on microstructural stability, Mo may be beneficial to Cr-lean, Al and Ti containing CCA design space, particularly as such alloys have often been shown to have multi-phase microstructures vulnerable to

Journal Pre-proof

localized corrosion at phase interfaces [15, 18, 21, 50]. Thus, it is necessary to evaluate the effect of Mo on the corrosion and passivity of such CCAs to optimize compositions.

This work investigates three $Al_{0.3}Cr_{0.5}Fe_2Mo_xNi_{1.5}Ti_{0.3}$ (x = 0, 0.05, 0.15) containing CCAs of FCC + $L2_1$ microstructure from a CCA alloy system designed and optimized for mechanical strength, ductility, and toughness [51]. The concentration of Mo is adjusted to evaluate the optimal concentrations for passivation and corrosion resistance in an alloy system that is dependent on three elements (Al, Cr, and Ti) for passivity [7], as opposed to traditional alloys such as stainless steels with high Cr content and Cr-dominated passive films [52]. The effects on phase content, passive film chemical composition, and elemental dissolution are observed with X-ray diffraction (XRD) and SEM, XPS and atomic emission spectroelectrochemistry (AESEC) respectively. While minimizing Mo concentration may decrease alloy cost and density, as well as improve compositional homogeneity, concentrations below a critical threshold may leave the alloys vulnerable to localized corrosion. The determining factors for compositional optimization and the role of Mo in the passivation and corrosion process will be discussed.

Experimental Methods

Three CCAs with the compositions $Al_{0.3}Cr_{0.5}Fe_2Mo_xNi_{1.5}Ti_{0.3}$ (x = 0, 0.05, 0.15) listed in Table I, henceforth referred to as Mo-0, Mo-1.1, and Mo-3.2 with regards to Mo concentrations in at. %, were synthesized via arc melting into a water-cooled copper hearth under Ar cover gas from high purity (greater than 99.9%, Cr greater than 99.2 %) elements. Compositions were selected based on pervious work in similar systems targeting light-weight, low-cost, corrosion resistance CCAs [7, 18, 51] and were predicted to have an FCC matrix with Heusler ($L2_1$) second phases with computational methods discussed elsewhere [51, 53]. Samples were remelted and flipped five times to ensure chemical homogeneity before being suction cast in a copper mold to produce disk-shape samples with 5 mm thickness and 10 mm diameter. Cast samples were encapsulated under Ar into quartz tubes and annealed for five hours at 1070 °C before

Journal Pre-proof

quenching in water. Samples were mechanically ground with SiC paper up to 1200 grit and, in the case of microstructural and surface chemistry analysis, polished with polycrystalline suspension through 0.25 microns before cleaning with acetone and isopropyl alcohol.

Table I: *Nominal CCA and 316L compositions in atomic percent. Pure elements were massed within 1% error of the tabulated compositions prior to arc melting. The 316L compositions are defined as the median of the acceptable range and also include minor amounts of C, N, P, S, and/or Si.*

Alloy	Al	Cr	Fe	**Mo**	Ni	Ti
Mo-0	6.5%	10.9%	43.5%	**0.0%**	32.6%	6.5%
Mo-1.1	6.5%	10.8%	43.2%	**1.1%**	32.3%	6.5%
Mo-3.2	6.3%	10.5%	42.1%	**3.2%**	31.6%	6.3%
316L	0.0%	17.0%	68.5%	**2.5%**	12.0%	0.0%

Phases present in the microstructure were identified with XRD using Cu Kα X-rays (1468.7 eV) at a scan rate of 0.15 °/s on a PANalytical Empyrean Diffractometer™ using Bragg-Brentano focusing geometry. The optics used were a 4 mm mask, 0.25° divergence slit, 1.52 mm anti-scatter slit, and 1.15° Soller slit on the incident beam side with a 16.8 mm anti-scatter slit and 2.3° Soller slit on the diffracted beam side. The microstructure was imaged with SEM on an FEI Quanta 650™ in backscattered electron (BSE) imaging mode at an accelerating voltage of 15 keV, a probe size of approximately 4 nm, and a working distance of approximately 10 mm. Energy dispersive spectroscopy (EDS) was utilized in both point scan and mapping mode to evaluate phase composition and was analyzed with Oxford Instruments Aztec™ software. Phase fractions were approximated from brightness threshold analysis of the BSE micrographs via ImageJ.

A conventional three-electrode cell connected to a Gamry Instrument Reference 600+™ potentiostat was utilized for electrochemical testing with the sample as the working electrode, a platinum mesh counter electrode, and a saturated calomel reference electrode (SCE) relative to which all potentials

Journal Pre-proof

hereafter are reported. An area of 0.1 cm^2 was exposed via a rubber O-ring to electrolyte solutions of 0.1 M NaCl adjusted to both pH 4 and 10 with concentrated HCl and NaOH respectively to evaluate corrosion behavior over a range of environments with differing stability levels of Mo. The electrolyte was continually bubbled with $N_{2(g)}$ throughout testing to reduce the activity of dissolved oxygen. All samples were compared to a commercially procured (North American Steel) 316L stainless steel (UNS S31600) control of a comparable Mo concentration (2-3 at. %). Three procedures were utilized to provide a comprehensive analysis of the passivity and corrosion resistance of the alloys.

The solution-exposed air-formed oxide film was electrochemically characterized by measuring the open circuit potential (OCP) for 1800 s directly after grinding. OCP measurement was followed by electrochemical impedance spectroscopy (EIS) at the final OCP measured between frequencies of 1 MHz and 5 mHz with 8 points/decade and an applied AC potential of 20 mV_{rms}. EIS spectra were fit to a Randles circuit modified to include a constant phase element (CPE) with Gamry Echem Analyst software™. The procedure was repeated after 20-day immersion in 0.1 M NaCl pH 4 alongside mass loss measurements. Surfaces for each alloy were then imaged with SEM in BSE mode.

Second, to observe the passivation behavior, the air-formed oxide was first exposed to a cathodic reduction treatment by applying a -1.3 V_{SCE} potential for 600 s, which has been shown in previous work to adequately minimize the air-formed oxide in similar CCAs via in-situ impedance measurements [7, 18, 54]. The sample was then potentiodynamically polarized in the forward direction from -1.3 to +0.8 V_{SCE} at a scan rate of 0.5 mV/s followed by a reverse scan (+0.8 to -1.3 V_{SCE}, 0.5 mV/s). To analyze the polarization behavior in the absence of localized corrosion, the procedure was repeated in 0.1 M Na_2SO_4 with the pH adjusted to 4 and 10 with concentrated H_2SO_4 and NaOH respectively. Finally, an oxide film was grown in the passive range by first exposing the sample to the -1.3 V_{SCE} cathodic treatment and then applying a potential step to -0.2 V_{SCE} for 10 ks. The potential was determined to be in the passive range by initial potentiodynamic polarization testing. Following the potentiostatic hold, a potentiostatic EIS experiment

Journal Pre-proof

was carried out at an applied potential of -0.2 V_{SCE} (1 MHz to 5 mHz, 8 points/decade, 20 mV_{rms}, modified Randles circuit fitting) before OCP was recorded for 1800 s. All electrochemical experiments were repeated threefold to ensure reproducibility. The pitting potential (E_{pit}) in NaCl was defined at the potential for which anodic current densities exceeded 10^{-4} $A.cm^{-2}$ with abrupt change in slope. Statistically distributed properties obtained during potentiodynamic polarization testing in chloride solutions such as pitting and repassivation potentials necessitated additional replication. Cumulative probability plots were developed in accordance with ASTM G16-95[2] [55] with methods previously adapted to characterize localized corrosion in Ni-based Mo-containing alloys [56, 57].

To identify the fate of individual elements in passivation and dissolution, AESEC was utilized on Mo-3.2 and pure Mo samples during the polarization and potentiostatic film growth procedures described above. The electrolyte solution containing dissolved elements was transported to a Horiba Jobin Yvon Ultima 2C^{TM} inductively coupled plasma atomic emission spectrometer (ICP-AES) via a flow cell. Elemental dissolution rates were evaluated by monitoring emission intensity at a characteristic wavelength for each element. A polychromator at a focal length of 0.5 m was utilized alongside a monochromator used to obtain a better signal resolution of Mo, Cr or Al depending on the electrolyte condition. To compare to electron current density (j_e), elemental dissolution rates were converted to an equivalent current density (j_M) with Faraday's law. A more thorough scientific basis and methodology for AESEC analysis is available elsewhere [58]. Dissolution rates in Ar-deaerated 0.1 M NaCl pH 4 and 0.1 M NaCl pH 10 were monitored during potentiodynamic polarization from -1.3 to +1.0 V_{SCE} (0.5 mV/s) following a 600 s exposure to OCP and a 600 s cathodic treatment at -1.3 V_{SCE}. Additionally, dissolution rates were monitored during potentiostatic passive film formation (-0.2 V_{SCE}, 4 ks) directly after exposure to OCP, bypassing any

[2] For the passive current density probability plots, the procedure was modified to take the linear regression from the logarithm of the current densities.

Journal Pre-proof

cathodic reduction. The test time was decreased relative to previous electrochemical tests to ensure plasma stability.

XPS was utilized to characterize the passive film composition and valence. Each sample was exposed to a 600 s cathodic treatment at -1.3 V_{SCE} followed by a 10 ks potentiostatic hold at -0.2 V_{SCE}, the potential and time used for the potentiostatic oxide growth procedure described above. Samples were transported under $N_{2(g)}$ directly to a PHI VersaProbe III™ XPS system, bypassing any EIS and OCP measurement. Al Kα X-rays (1468.7 eV) at a 26 eV pass energy, 45° take off angle, and with a 100 µm spot size[3] were used. High resolution spectra were collected over the Al 2p, Cr $2p_{3/2}$, Fe $2p_{1/2}$, Mo 3d, Ni $2p_{3/2}$, and Ti $2p_{3/2}$ core series with spectra bounds defined by an initial survey scan. Spectra were calibrated with C 1s set to 284.8 eV and deconvoluted with a Shirley background correction, Doniach-Sunjic peaks for metallic features, and Voigt functions for oxidized features with KOLXPD™ analysis software. Peak deconvolutions were constrained by position, full-width half maximum, and multiple splitting utilizing spectra of known reference compounds obtained elsewhere [59-62]. As Ni Auger peaks overlap the Fe $2p_{3/2}$ core series, a constant position shift between the experimentally obtained Fe $2p_{1/2}$ series and reference spectra in the Fe $2p_{3/2}$ series was assumed to identify chemical species. The intensity of the Cr 3s series, which overlaps the Al 2p series, was fixed based on the intensity of the Cr $2p_{3/2}$ series adjusted with relative sensitivity factors. Cation fractions were evaluated as the proportion of the intensities of the oxidized states for each element normalized with relative sensitivity factors with methods discussed further in the supplementary information section. Multi-cation species (e.g. spinels) are only suggested

[3] The XPS spot size is significantly larger than any second phase regions, limiting the ability to evaluate the lateral variation in passive film chemistry with regards to the bulk phase over which the film was grown. XPS measurements are obtained over a large enough area that they may be reasonably assumed to be representative of the entirety of the microstructure. High-resolution evaluation of the passive film chemistry with regards to phase interfaces in the microstructure will form the basis for a future study.

Journal Pre-proof

for alloys for which good fit agreement is obtained when fit to both core series with the peak intensity constrained by fixing cation fractions for each species to stoichiometric ratios between each element.

Results

Characterization of Alloy Microstructure

The CCAs are suggested by XRD patterns shown in Figure 1 to have a predominantly FCC microstructure with a second phase also detected. The second phase has been suggested to be $L2_1$ using methods discussed elsewhere [51]. Figure 2 indicates second-phase regions are of single-micrometer size. The phase volume and morphology is similar across all three CCAs with Mo-1.1 and Mo-3.2 having slightly higher $L2_1$ volume fractions than Mo-0.

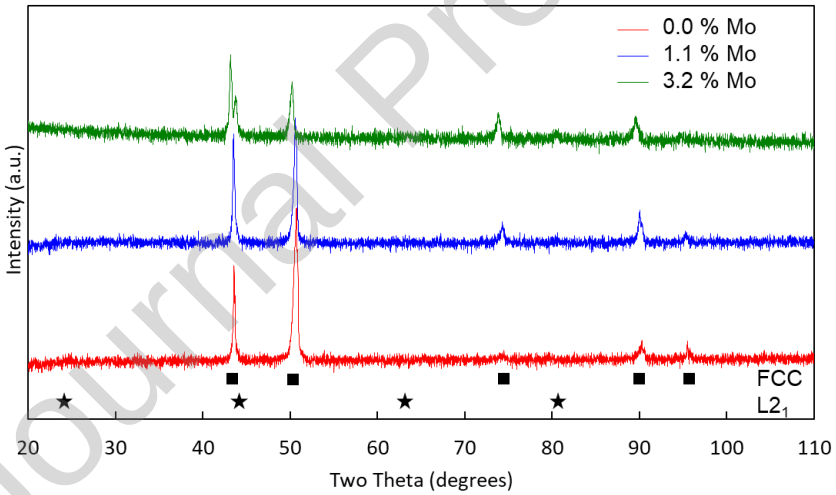

Figure 1: *XRD patterns for synthesized and homogenized CCAs. Square and star indexes identify corresponding diffraction peaks for FCC and $L2_1$ phases respectively.*

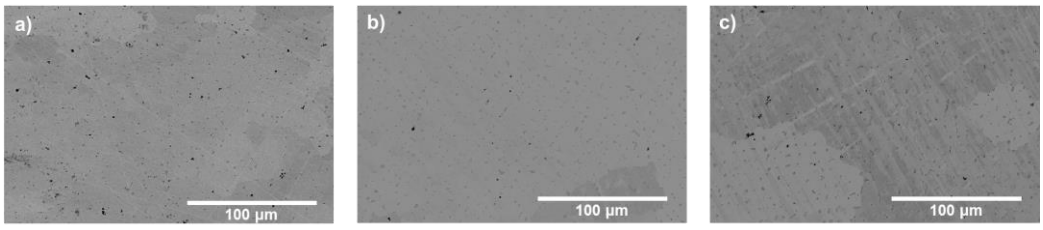

Figure 2: *BSE micrographs of a) Mo-0, b) Mo-1.1, and c) Mo-3.2 microstructures*

Journal Pre-proof

EDS point scans for each CCA (Table II) and mapping for the Mo-3.2 alloy (Figure 3) both suggest the matrix to be enriched in Fe, Cr, and Mo, while the second phase is enriched in Al, Ti, and Ni with each element present in both phases. Generally, the degree of Al and Ti partitioning increases with Mo content, with Mo-0 exhibiting the most chemically homogenous microstructure with regards to the ratios between the concentrations of each element in the FCC matrix compared to $L2_1$ EDS point scans. EDS mapping of additional CCAs is shown in the supplementary information section.

Table II: *Elemental fractions obtained from EDS point scans over matrix and second phase regions of each CCA and area fractions obtained via ImageJ analysis of a series of BSE micrographs.*

Phase	Al	Cr	Fe	Mo	Ni	Ti	Area
			Mo-0				
Matrix	7.8	13.5	52.8	-	18.6	7.3	96.9%
2nd Phase	18.7	4.3	18.9	-	42.5	15.6	3.1%
			Mo-1.1				
Matrix	6.1	11.5	44.1	1.3	31.1	5.9	95.6%
2nd Phase	20.5	2.3	13.4	Trace	45.1	18.7	4.4%
			Mo-3.2				
Matrix	3.7	11.6	44.7	3.2	30.7	6.1	96.0%
2nd Phase	15.3	2.5	13.9	0.5	47.3	20.5	4.0%

Journal Pre-proof

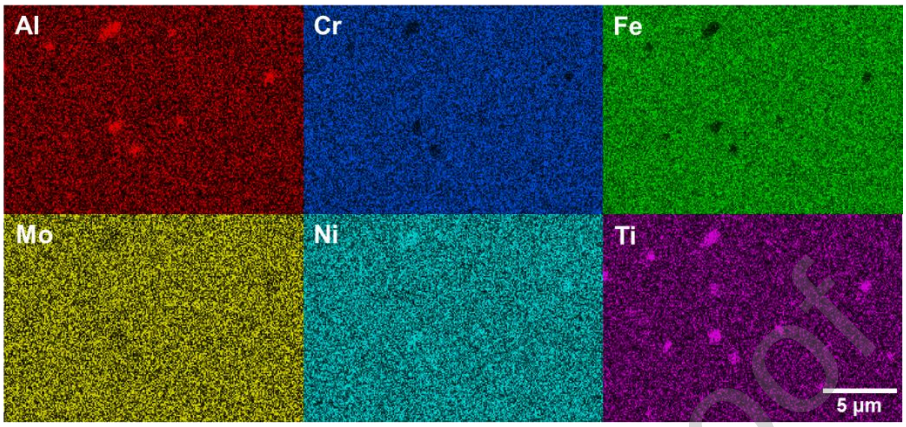

Figure 3: *EDS mapping of representative second phase regions within the Mo-3.2 microstructure*

Characterization of Passivity and Transpassive Breakdown by Potentiodynamic Polarization in Cl^- Free Electrolytes

E-log(i) curves obtained in acidic and basic Na_2SO_4 solutions, which allow for characterization of the passivation process without Cl^- induced breakdown, are shown in Figure 4. Extracted parameters are summarized in Table S.1. All materials passivate either spontaneously or after an active to passive transition, although no clear trends are present regarding the critical current density and critical potential. Critical current densities and potentials are further obscured by changes in sign of the current density prior to the formation of a stable passive film for Mo-0 in pH 4 and Mo-1.1 in pH 10. In both environments, Mo-1.1 has the highest passive current density (i_{pass}). i_{pass} of Mo-0 is comparable to that of 316L in the pH 4 solution, but 316L has a lower i_{pass} than all CCAs at pH 10. Increasing current densities representative of transpassive dissolution of the passive film are not observed within the evaluated potential range for any of the CCAs. However, such behavior is suggested for the Al and Ti-free 316L at potentials above 0.6 V_{SCE}. No trends in corrosion potential (E_{corr}) are observable.

Journal Pre-proof

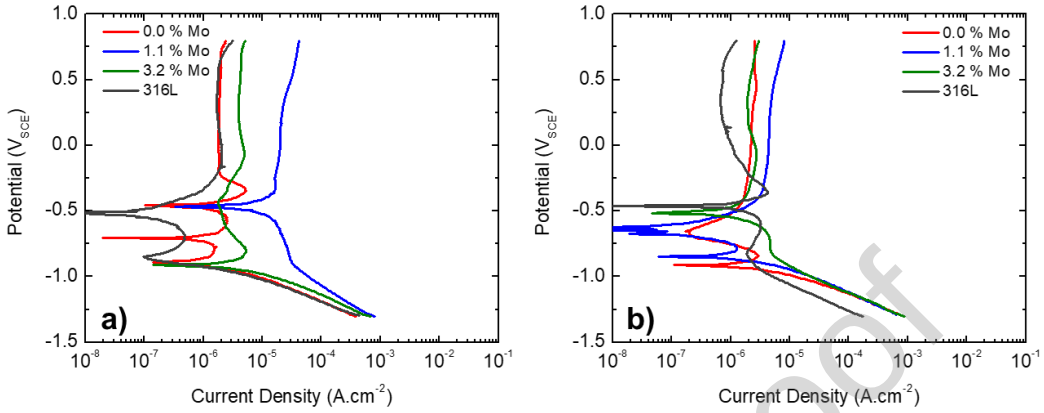

Figure 4: *Potentiodynamic polarization of CCAs and 316L in $N_{2(g)}$ bubbled a) 0.1 M Na_2SO_4 pH 4 and b) 0.1 M Na_2SO_4 pH 10 following cathodic reduction pre-treatment (600 s, − 1.3 V_{SCE}).*

Characterization of Passivity and Localized Breakdown by Potentiodynamic Polarization in Cl^- Containing Electrolytes

Figure 5 shows representative E-log(i) curves in acidic and basic NaCl solutions and selected probability plots with key parameters quantified in Table III. E_{corr} generally increases with increased Mo concentration in the pH 4 solution. Opposite trends are seen in the pH 10 solution, potentially driven by the solubility of MoO_4^{2-} in basic environments and resultant dissolution and depletion of Mo from the oxide [63]. i_{pass} is lower in pH 10 than in pH 4 for all CCAs with the lowest values observed for Mo-0 in pH 4 and similar values for each CCA in pH 10. Probability plots for E_{corr} and i_{pass} are shown in Figure S.2.

Journal Pre-proof

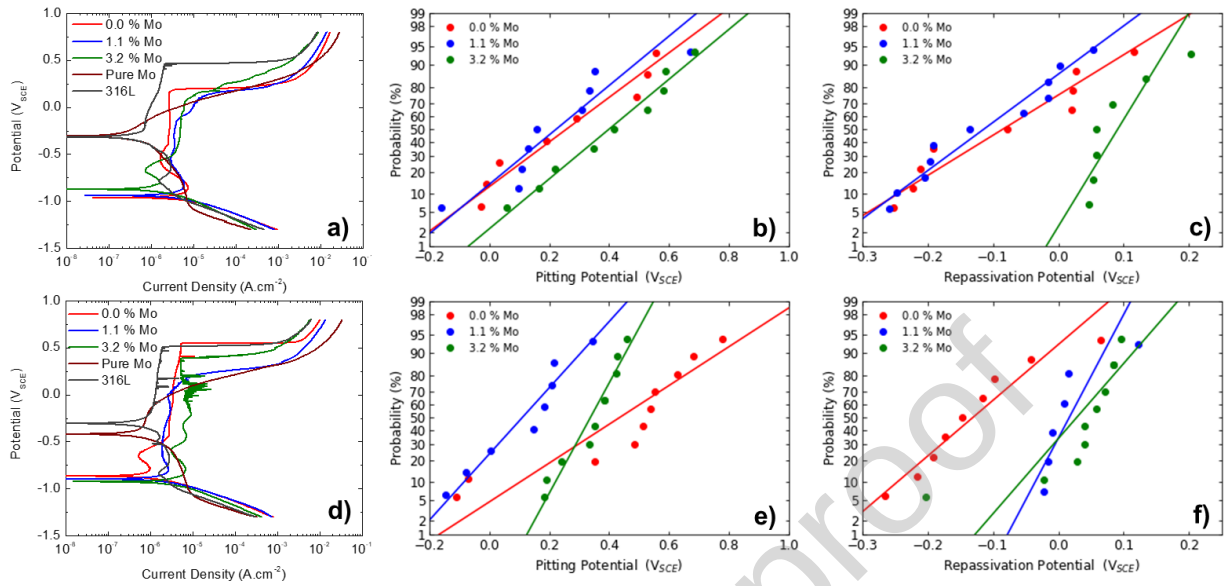

Figure 5: *a,d) E-log(i) and cumulative probability plots for b, e) pitting potential and c, f) repassivation potential summarizing potentiodynamic polarization of CCAs, pure Mo, and 316L in $N_{2(g)}$ bubbled a,b,c) 0.1 M NaCl pH 4 and d,e,f) 0.1 M NaCl pH 10 following cathodic reduction pre-treatment (600 s, − 1.3 V_{SCE}).*

Table III: *Selected corrosion parameters for potentiodynamic polarization shown in Figure 5 obtained in a) 0.1 M NaCl pH 4 and b) 0.1 M NaCl pH 10. Each term includes the mean value bounded by a one standard deviation range.*

a)	0.1 M NaCl pH 4			
Alloy	E_{corr} (V_{SCE})	E_{pit} (V_{SCE})	E_{rep} (V_{SCE})	i_{pass} ($\mu A.cm^{-2}$)
Mo-0	-0.827 +/- 0.194	0.256 +/- 0.231	-0.086 +/- 0.129	6.88 +/- 2.13
Mo-1.1	-0.767 +/- 0.238	0.222 +/- 0.218	-0.115 +/- 0.106	16.78 +/- 15.55
Mo-3.2	-0.501 +/- 0.285	0.399 +/- 0.204	0.091 +/- 0.053	13.76 +/- 13.98
316L	-0.372 +/- 0.062	0.465 +/- 0.008	-0.072 +/- 0.079	0.18 +/- 0.05

Journal Pre-proof

b)	0.1 M NaCl pH 10			
Alloy	E_{corr} (V_{SCE})	E_{pit} (V_{SCE})	E_{rep} (V_{SCE})	i_{pass} ($\mu A.cm^{-2}$)
Mo-0	-0.627 +/- 0.237	0.435 +/- 0.285	-0.131 +/- 0.094	5.38 +/- 2.96
Mo-1.1	-0.675 +/- 0.26	0.11 +/- 0.157	0.016 +/- 0.049	4.86 +/- 3.93
Mo-3.2	-0.852 +/- 0.153	0.338 +/- 0.094	0.028 +/- 0.084	6.59 +/- 5.31
316L	-0.307 +/- 0.004	0.431 +/- 0.111	-0.019 +/- 0.004	0.130 +/- 0.028

All three CCAs generally have lower localized corrosion resistance than 316L in the Cl^--containing solutions, with passive films breaking down by pitting and limited crevice corrosion. The repassivation potentials (E_{rep}) obtained from downward scans, such as those shown in Figure S.2, indicate the presence of positive trends with increasing Mo concentration. Although the distribution of E_{rep} increases from Mo-0 to Mo-3.2 in both environments, Mo-1.1 has a similar distribution to Mo-0 in the pH 4 environment whilst it is similar to that of Mo-3.2 in the pH 10 environment. Similar trends are shown for the E_{pit} in the pH 4 environment, with the E_{pit} increasing by nearly 0.15 V from Mo-0 to Mo 3.2. The increase suggests Mo increases the resistance of the passive film to localized breakdown or that the stabilization and propagation stages are affected. However, E_{pit} is higher for Mo-0 in the pH 10 environment, deviating from the trends established for E_{rep} and E_{pit} in the pH 4 environment. Neither E_{pit} nor E_{rep} are affected to a statistically significant level by pH, with the notable exception of the increased E_{pit} of Mo-0 in the pH 10 solution. Intermediate spikes before breakdown in the E-log(i) curves, most noticeably those of Mo-3.2 and 316L, suggest breakdown and repassivation due to metastable pitting. Neither the passivation nor breakdown behavior of any of the CCAs resembled that of pure Mo.

Journal Pre-proof

AESEC was utilized to track individual elemental dissolution rates during upward polarization of the Mo-3.2 alloy (Figure 6). The elemental dissolution rates are presented in equivalent current densities with the oxidation states used to calculate them indicated in the parenthesis. At both pH 4 and pH 10, elemental dissolution rates are mostly below the detection level at potentials in the passive regime (approximately -0.45 to -0.20 V_{SCE} for pH 4 and -0.8 to -0.15 V_{SCE} for pH 10). For example, at pH 4, Ni and Fe begin to dissolve at potentials near E_{pit} (-0.07 V_{SCE}) while other elements dissolve at more positive potentials (0.07 V_{SCE} for Cr, 0.17 V_{SCE} for Mo, Al, and Ti). At higher potentials (above 0.0 V_{SCE}), the elemental dissolution rates are not proportional to the composition of either phase.

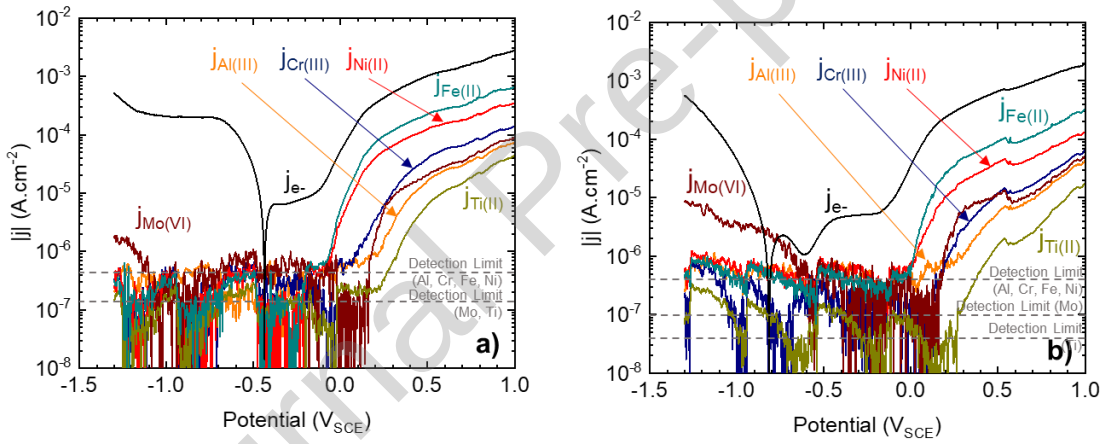

Figure 6: *Equivalent current densities of in-situ elemental dissolution rates monitored via AESEC during upward polarization of Mo-3.2 in $N_{2(g)}$ bubbled a) 0.1 M NaCl pH 4 and b) 0.1 M NaCl pH 10. Dashed lines indicate element detection limits.*

The Mo-3.2 elemental dissolution rates within the transpassive region calculated from the equivalent current densities are presented in Table IV. Only the Ni and Fe compositions were remarkably different in that the dissolved Ni was lower than the expected alloy composition (31.6 at. % Ni), and the dissolved Fe (53.6% for pH 4 and 58.5% for pH 10) was higher than the alloy composition (42.1 at. % Fe) in both pHs. Lower Mo contents than the expected alloy composition from Table I (3.2 at. % Mo) indicate slight Mo enrichment.

Journal Pre-proof

Table IV: *Proportion of transpassive elemental dissolution attributable to each element in at. %. Values are determined from the ratios of equivalent current densities obtained via AESEC at E = 1.0 V_{SCE} during LSV in 0.1 M NaCl at pH 4 and 10 shown in Figure 6. Bolded terms indicate dissolution rates higher than the bulk alloy composition suggesting depletion.*

Electrolyte	Al	Cr	Fe	Mo	Ni	Ti
0.1 M NaCl pH 4	4.1%	7.6%	**53.6%**	2.5%	28.6%	3.6%
0.1 M NaCl pH 10	4.0%	7.7%	**58.5%**	2.8%	23.8%	3.2%

Dissolution of Mo in the cathodic region is observed for both Mo-3.2 and pure Mo (Figure S.3) for both environments with significantly higher Mo dissolution rates in pH 10. The higher Mo dissolution in the cathodic potential range at pH 10 may be attributed to the dissolution of the pre-existing Mo-based corrosion products formed after mechanical grinding. A significantly high cathodic current density at the level of $-1*10^{-4}$ $A.cm^{-2}$ is observed for both Mo-3.2 (Figure 6a) and pure Mo (Figure S.3) at pH 4 with relatively low Mo dissolution rate compared to that at pH 10. Notably, Mo dissolution shows an increased Tafel slope relative to other elements for both pH 4 and pH 10.

Growth and Characterization of Passive Films by Impedance Spectroscopy

Figure 7 shows EIS characterization utilized to provide a more comprehensive electrochemical characterization of the air-formed solution-exposed passive films after 1800 s at OCP. All OCP values were within 80 mV of each CCA in the same environment, with no clear trends with Mo concentration. In all cases, EIS is acquired at potentials well within the passive region defined by Figure 5. In this preliminary report, the spectra for the CCAs and 316L were fit with the modified Randles circuit shown in Figure 7e with fit parameters shown in Table V. In this model the polarization resistance (R_P) likely encompasses both charge transfer resistance and diffusional impedance. In both acidic and basic environments, R_P decreases with Mo content relative to Mo-0. Despite the high R_P values, Mo-0 has a CPE coefficient (α)

Journal Pre-proof

below 0.8 in both pH environments, whereas the higher α values of other CCAs and 316L are indicative of more ideal capacitive behavior [64]. The corrosion resistance of the air-formed solution-exposed passive films of all CCAs are suggested to be inferior to the corrosion resistance of films formed on 316L based on lower R_P values obtained in both environments.

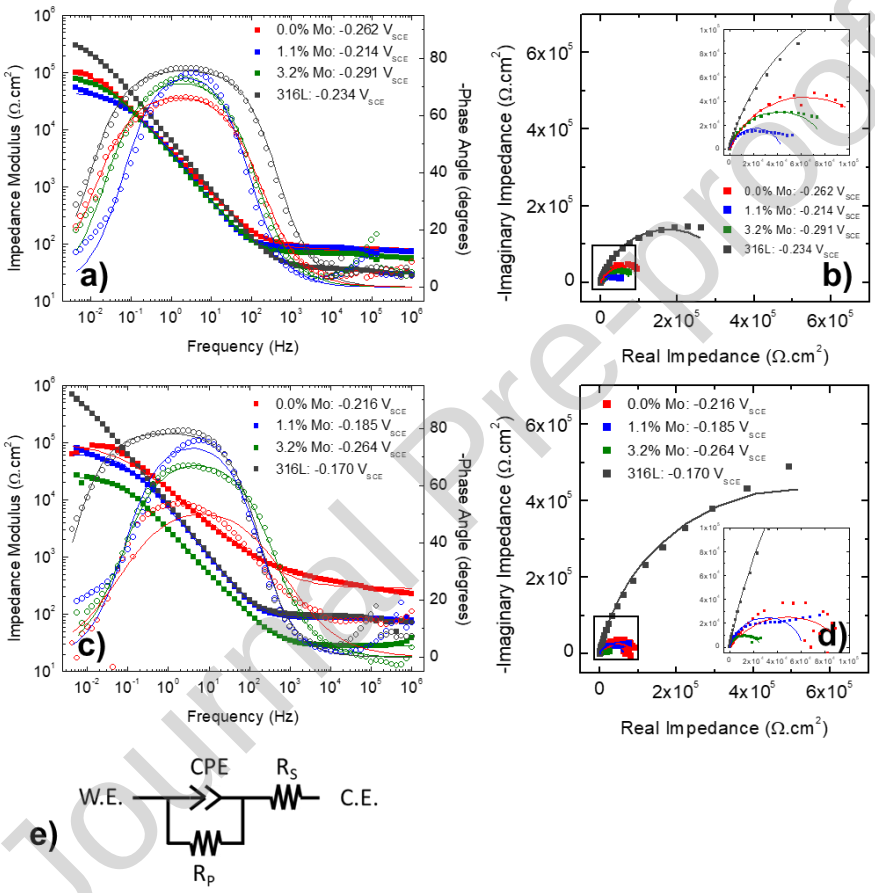

Figure 7: *a,c) Bode and b,d) Nyquist plots obtained following 30 minutes exposure of the air-formed oxides to open circuit corrosion in $N_{2(g)}$ bubbled a,b) 0.1 M NaCl pH 4 and c,d) 0.1 M NaCl pH 10. The final OCP values and potentials at which EIS was measured are indicated in the figure legends. e) Equivalent circuit model utilized for EIS fits*

Journal Pre-proof

Table V: *EIS fit parameters for the spectra shown in Figure 7 obtained in a) 0.1 M NaCl pH 4 and b) 0.1 M NaCl pH 10. Each term is defined by the Randles circuit shown in Figure 7e.*

a)	0.1 M NaCl pH 4			
Alloy	R_S ($\Omega.cm^2$)	R_P ($k\Omega.cm^2$)	Y ($\mu S.s^{\alpha}.cm^{-2}$)	α_f
Mo-0	81.1	126.7	55.6	0.766
Mo-1.1	80.4	43.4	51.6	0.864
Mo-3.2	63.5	82.7	59.2	0.824
316L	33.9	350.6	32.9	0.852

b)	0.1 M NaCl pH 10			
Alloy	R_S ($\Omega.cm^2$)	R_P ($k\Omega.cm^2$)	Y ($\mu S.s^{\alpha}.cm^{-2}$)	α_f
Mo-0	282.6	96.8	19.5	0.610
Mo-1.1	82.7	61.9	28.7	0.856
Mo-3.2	28.4	26.3	75.1	0.783
316L	82.6	1039.0	23.8	0.880

During 20-day immersion in 0.1 M NaCl adjusted to pH 4, Mo-1.1 has the highest mass loss rate (Table VI). Both Mo-0 and Mo-3.2 had lower mass loss rates by over an order of magnitude, indicating there were no clear trends with Mo concentration. Figure 8 shows film breakdown is attributable to pitting, with pits frequently observed at or near second phase interfaces. Neither phase is suggested to preferentially dissolve, nor do pits appear do penetrate into either phase at significantly higher rates. Furthermore, Figure 9 and Table VII show both the OCP and R_P values of Mo-1.1 and Mo-3.2 decrease during long-term immersion. Decreasing OCP values suggest the passive film is not improved by the extended exposure, while both values increase during the immersion for Mo-0 and 316L, indicating growth of a more protective passive film.

Journal Pre-proof

Table VI: *Mass loss and average area penetration rates obtained during 20-day immersion of CCAs and 316L in 0.1 M NaCl pH4. The mass gain observed for Mo-3.2 approached the tolerance of the scale and may be interpreted as negligible.*

Alloy	Mass Loss Rate ($mg.cm^{-2}.y^{-1}$)	Area Average Penetration Rate ($\mu m.y^{-1}$)
Mo-0	1.3	1.7
Mo-1.1	13.2	17.3
Mo-3.2	-0.1 (Trace)	-0.1 (Trace)
316L	0.8	1.0

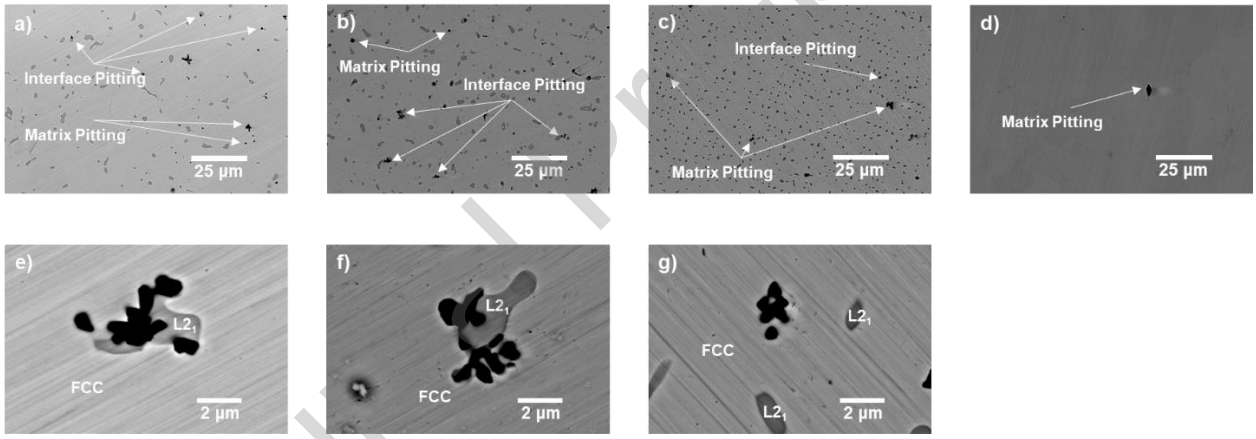

Figure 8: *BSE micrographs showing representative pit morphologies for a) Mo-0, b) Mo-1.1, c) Mo-3.2, and d) 316L. High magnification micrographs show pits formed on e) Mo-0, f) Mo-1.1, and g) Mo-3.2 with regards to second phase morphology.*

Table VII: *EIS fit parameters for the spectra shown in Figure 9 obtained following 20-day immersion in 0.1 M NaCl pH 4. Each term is defined by the Randles circuit shown in Figure 7e.*

	0.1 M NaCl pH 4: Day 20			
Alloy	R_S ($\Omega.cm^2$)	R_P ($k\Omega.cm^2$)	Y ($\mu S.s^{\alpha}.cm^{-2}$)	α_f
Mo-0	72.8	1206.0	28.4	0.877
Mo-1.1	69.2	27.1	97.4	0.811
Mo-3.2	84.2	45.8	68.8	0.895
316L	71.6	1679.0	27.1	0.895

Journal Pre-proof

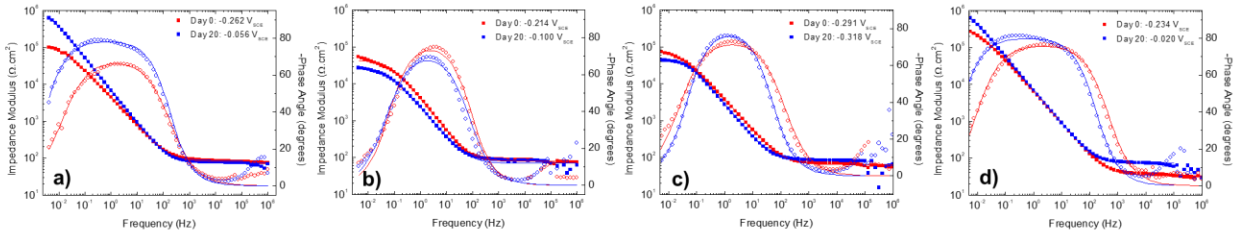

Figure 9: *Bode plots following 30 minutes and 20-day exposure to open circuit corrosion in 0.1 M NaCl pH 4 of the air-formed oxides formed on a) Mo-0, b) Mo-1.1, c) Mo-3.2, and d) 316L. Spectra were fit with the equivalent circuit model shown in Figure 7e. The final OCP values and potentials at which EIS was measured are indicated in the figure legends.*

A film grown in the passive region after cathodic treatment via applying a -0.2 V_{SCE} potential, indicated as part of the passive range of each CCA by initial potentiodynamic polarization (Figure 5), was also characterized. Figure 10 shows current density measurements throughout the passive film growth procedure. In pH 4 solution, the current density is generally higher in CCAs with less Mo beyond 100 s. A steady increase in the current density of Mo-0 suggests the formation of a weaker and/or dissolving passive film, although no pits or other features of localized corrosion were visible following exposure. In pH 10 solution, all current densities decrease with time and trends with Mo content are less prominent, with Mo-1.1 having the highest current density at the conclusion of the film growth procedure. Sharp decreases in current densities approaching zero occur on most alloys as anodic passivation approaches the residual oxygen reduction rate, indicating a transition from the anodic to cathodic regime. For both environments, 316L has lower current density magnitudes than all evaluated CCAs.

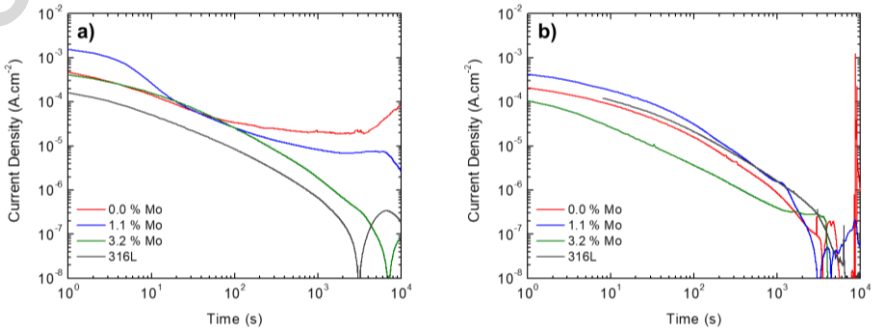

Figure 10: *Current densities of CCAs and 316L during exposure to a -0.2 V_{SCE} potential in $N_{2(g)}$ bubbled a) 0.1 M NaCl pH 4 and b) 0.1 M NaCl pH 10 following cathodic reduction pre-treatment (600 s, − 1.3 V_{SCE}).*

Journal Pre-proof

Individual elemental dissolution rates are measured during the potentiostatic film growth on Mo-3.2 via AESEC (Figure 11) in pH 4 and pH 10 solutions. Fe and Ni dissolve and followed similar trends as electron current density at pH 4 (Figure 11a), while dissolution rates of the other elements such as Al and Ti are generally below the detection limit. In pH 10 solution (Figure 11b), Mo slightly dissolves but does not reflect trends in the electron current density, particularly past 10^3 seconds. A slight increasing trend of Al dissolution rate with time is observed at pH 10 while those of Fe, Ni, Cr and Ti are below the detection limit.

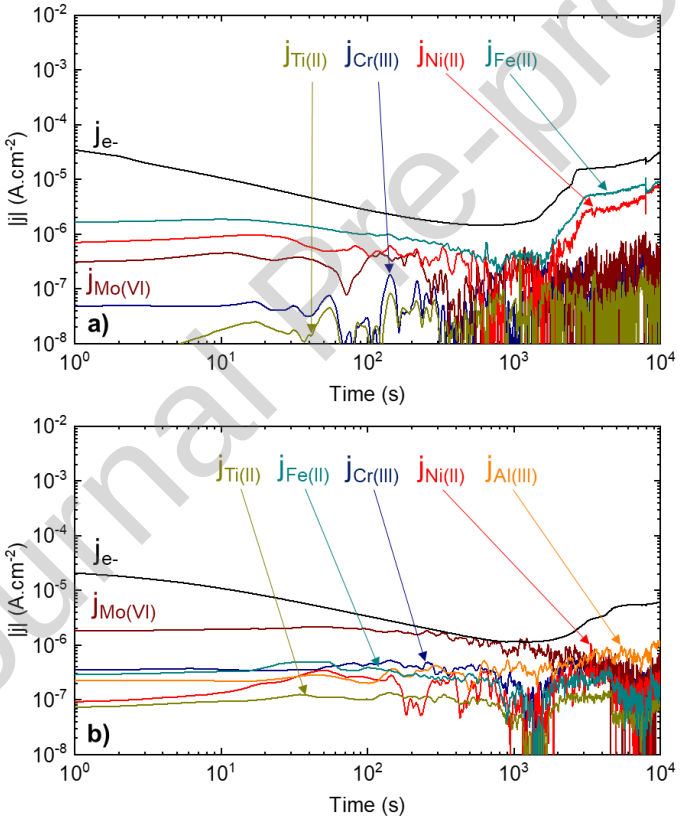

Figure 11: *Equivalent current densities of in-situ elemental dissolution rates monitored via AESEC during exposure of Mo-3.2 to a -0.2 V_{SCE} potential in $N_{2(g)}$ bubbled a) 0.1 M NaCl pH 4 and b) 0.1 M NaCl pH 10. Dashed lines indicate element detection limits. Al dissolution rates are not shown in pH 4 due to high amounts of noise.*

Following potentiostatic passive film growth, the films were characterized with EIS (Figure 12, Table VIII) and fit with the Randles circuit described above (Figure 7e). The high current density observed

Journal Pre-proof

during film growth (Figure 10a) is characteristic of a less corrosion resistant passive film. Unlike the case of the air-formed solution-exposed films, R_P increases with Mo content in both environments. α is above 0.85 for all alloys in both environments, indicating characteristic capacitive behaviour of the passive films. The R_P magnitude values vary less with Mo concentrations under pH 10 conditions than in pH 4 conditions, with much of the variability attributable to the low R_P of the film formed on Mo-0 in pH 4 conditions. R_P of all the CCA passive films is lower than that of 316L, regardless of Mo concentration or pH.

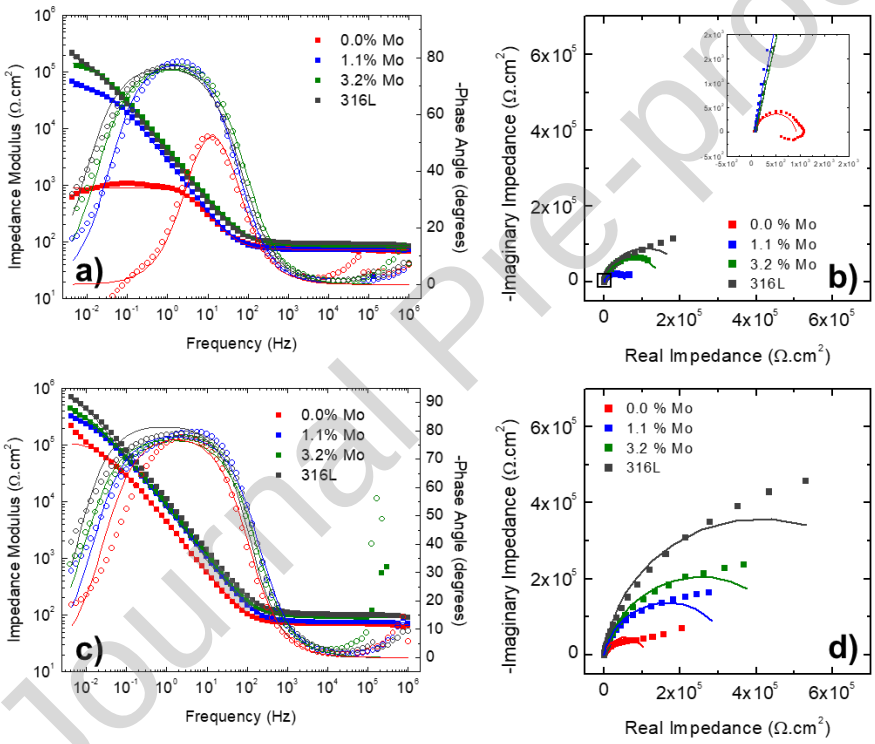

Figure 12: *a,c) Bode and b,d) Nyquist plots obtained following cathodic reduction pre-treatment (600 s, −1.3 V_{SCE}) and 10 ks exposure to -0.2 V_{SCE} in $N_{2(g)}$ bubbled a,b) 0.1 M NaCl pH 4 and c,d) 0.1 M NaCl pH 10. Spectra were fit with the equivalent circuit model shown in Figure 7e.*

Journal Pre-proof

Table VIII: *EIS fit parameters for the spectra shown in Figure 11 obtained in a) 0.1 M NaCl pH 4 and b) 0.1 M NaCl pH 10. Each term is defined by the Randles circuit shown in Figure 7e.*

a)	0.1 M NaCl pH 4			
Alloy	R_S ($\Omega.cm^2$)	R_P ($k\Omega.cm^2$)	Y ($\mu S.s^{\alpha}.cm^{-2}$)	α_f
Mo-0	73.3	0.8	74.9	0.917
Mo-1.1	72.2	56.4	69.9	0.902
Mo-3.2	87.0	153.4	45.6	0.871
316L	91.4	218.7	54.5	0.871

b)	0.1 M NaCl pH 10			
Alloy	R_S ($\Omega.cm^2$)	R_P ($k\Omega.cm^2$)	Y ($\mu S.s^{\alpha}.cm^{-2}$)	α_f
Mo-0	68.3	109.4	46.0	0.884
Mo-1.1	72.8	330.7	25.5	0.884
Mo-3.2	91.4	504.5	25.1	0.868
316L	95.5	818.0	24.1	0.918

Characterization of Passive Film Cation Fractions

XPS was utilized to characterize the passive films grown at -0.2 V_{SCE} with cation fractions of constituent elements in the passive films shown in Figure 13 and Table IX. For all CCAs and growth conditions, Cr(III), Ti(IV), and (in the case of Mo-1.1 and Mo-3.2) Mo(IV)/Mo(VI) are present in the passive film at higher concentrations than their respective bulk compositions. Fe(II)/Fe(III) and Ni(II) are depleted in the passive film relative to alloy content for all cases. Al(III) is present for all CCAs, but depleted in the film compared to the bulk in the Mo-0 alloy at pH 4 and the Mo-3.2 alloy at pH 10. For all CCAs, Cr(III) is the most prominent constituent in the passive film. However, the concentration of Cr(III) in the passive film decreases both with Mo concentration and pH. Although Fe(II)/Fe(III) and Ni(II) remained depleted in the film grown on Mo-3.2 at pH 10 relative to bulk composition, the surface cation fractions increased relative to the film grown at pH 4. Such increases were compensated by decreases in Al(III), Cr(III),

Journal Pre-proof

Mo(IV)/Mo(VI), and Ti(IV), suggesting the film more closely resembles bulk alloy composition. However, such decreases do not necessarily suggest instability of such elements in basic conditions.

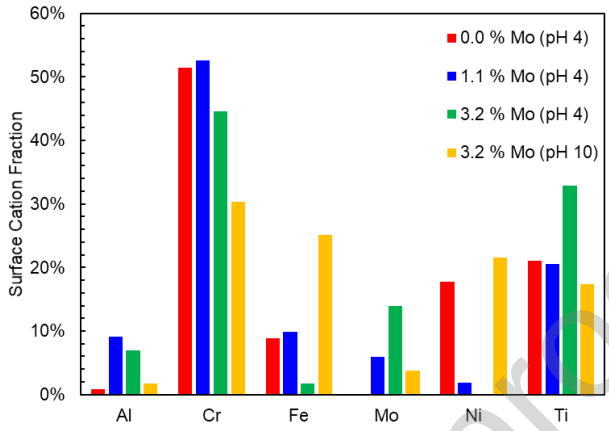

Figure 13: *Surface cation fractions calculated from XPS characterization of CCA passive films formed during 10 ks exposure to -0.2 V_{SCE} in 0.1 M NaCl pH 4 and 0.1 M NaCl pH 10 following cathodic reduction pre-treatment (600 s, – 1.3 V_{SCE}).*

Table IX: *Surface cation fractions obtained from the XPS fits shown in Figure 14. Bolded terms indicate surface cation fractions higher than the bulk alloy composition suggesting enrichment.*

Alloy	Al	Cr	Fe	Mo	Ni	Ti
Mo-0 pH 4	0.9%	**51.4%**	8.9%	0.0%	17.8%	**21.0%**
Mo-1.1 pH 4	**9.1%**	**52.6%**	9.9%	**5.9%**	1.9%	**20.6%**
Mo-3.2 pH 4	**6.9%**	**44.6%**	1.7%	**13.9%**	0.0%	**32.9%**
Mo-3.2 pH 10	1.7%	**30.4%**	25.1%	**3.8%**	21.6%	**17.4%**

Figure 14 shows fit XPS spectra for Cr, Mo, and Ni. Spectra for Al, Fe, and Ti along with precise fit parameters for all elements are shown in the supplementary information section. For all spectra, features characteristic of oxidized species as both hydroxides and oxides, as well as unoxidized metal are present, indicating the film is thin enough to permit observation of an attenuated signal from the bulk metal. Deconvolution of the Cr spectra suggests the presence of Cr(III) oxides, hydroxides, and that complex

Journal Pre-proof

oxides such as possible spinels ($FeCr_2O_4$ and $NiCr_2O_4$) cannot be ruled out in the passive film. The fitting suggests formation of a Cr-Ni spinel may contribute to the stability of Ni(II) and Cr(III) in the passive film formed in the pH 10 environment, although the chemical shifts, which are determined by local interactions, are insufficient to determine long-range structure. The surface cation fraction of Ni(II) increases with a decrease in Mo concentration in pH 4, with the Cr-Ni spinel no longer suggested for Mo-3.2 in pH 4. In addition to Cr(III), significant concentrations of Ti are present as Ti(IV) oxide. The Mo signal collected from the passive film of Mo-3.2 grown at pH 4 is nearly entirely attributable to the Mo(VI) valence while the film formed at pH 10 has a lower Mo surface cation fraction with a larger proportion attributable to Mo(0) and Mo(IV) valences. The 13.9 at. % surface cation fraction for Mo on the Mo-3.2 film formed at pH 4 suggests a significant role of Mo in the passivation process. Additionally, the film contains more Fe and Ni, and less overall Mo when grown in pH 10 solution than in pH 4, consistent with oxide and hydroxide thermodynamic stability. These results follow those shown by AESEC, where Fe and Ni dissolution rates were below the detection limit while Mo dissolution was observed at pH 10 (Figure 11b). At pH 4, only Fe and Ni dissolution is observed (Figure 11a), which is in agreement with the comparatively lower Fe(II)/Fe(III) and Ni(II) cation fractions in the passive film. In summary, while the films are consistently enriched in passive species predicted to be thermodynamically stable, Mo concentration plays a prominent role in altering the amount of each species.

Journal Pre-proof

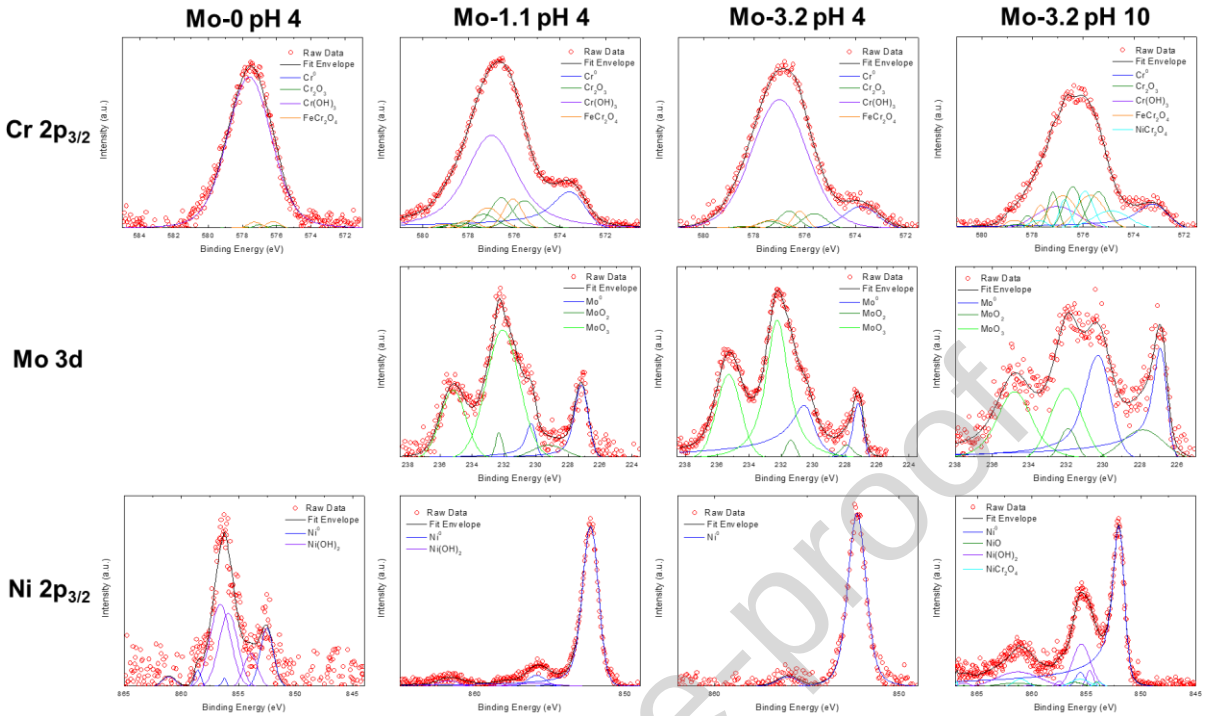

Figure 14: *XPS spectra of CCA passive films formed during 10 ks exposure to -0.2 V_{SCE} in 0.1 M NaCl pH 4 and 0.1 M NaCl pH 10 following cathodic reduction pre-treatment (600 s, − 1.3 V_{SCE}).*

Discussion

The selected alloys evaluate the effects of Mo additions from 0-3.2 at. % within the Al-Cr-Fe-Ni-Ti CCA systems. The alloying strategy preserves the ratios between passivating elements Al, Cr, and Ti and the composition of each of the three elements varies by less than 0.5 at. % between the CCAs (Table I). Thus, effects on corrosion resistance are attributable to Mo content. Furthermore, the Cr concentration of the investigated alloys was kept below critical thresholds for passivation in Fe-Cr (~13 at. % Cr [65]) and Ni-Cr (~12 at. % Cr [66]) alloys with Al and Ti also maintained below traditional Fe binary thresholds (~15 at. % Al [67], >47 at. % Ti [68]). Passivity below such Fe-Cr thresholds has been shown to be obtainable due to the addition of Al and Ti [7] with the optimal Al-Cr ratio informed by work in similar CCA systems [69].

The present study probes the effect of Mo alloying in the passive film (i.e., in Na_2SO_4), pit stabilization, and passive film growth in NaCl solutions at pH 4 and 10. Mo is present in the alloys mainly

Journal Pre-proof

in the FCC matrix (Table II) and is suggested by XPS to be present in Mo(0), Mo(IV), and Mo(VI) valence states (Figure 14). Utilization of pH 4 and 10 solutions further compares the effect of Mo with different thermodynamically expected fates (solid state stability versus dissolved aqueous anions) [63]. Stable or metastable Mo oxides are suggested in the oxide at anodic potentials near pH 4 whilst at pH 10, E-pH diagrams suggest Mo to be thermodynamically stable as MoO_4^{2-} [63]. This implies that Mo may operate to inhibit pitting in its traditional function as a dissolution suppressor. However, the presence of multiple valence states introduces the possibility of aliovalent Mo doping in the passive film that can create more ionic defects which may affect passive film dissolution separate from pitting phenomena [27]. Corrosion resistant passive film formation at OCP is found to exhibit the best attributes for the solution-exposed air-formed Mo-0 passive film (Figure 7, Table V). For instance, R_P of the Mo-0 solution-exposed air-formed oxide is higher following 20-day immersion (Figure 9a, Tables V, VII) and the mean i_{pass} in chloride is generally the lowest of the evaluated CCAs in this work (Figure 5, Table III). In contrast, Mo-3.2 is suggested to be the most corrosion resistant with regards to pitting susceptibility indicated by the most positive pitting potential at pH 4 (Figure 5, Table III).

Effect of Mo on Microstructural Partitioning and Localized Breakdown

Both the average E_{pit} and probabilistic distribution suggest improved resistance to film breakdown under acidic conditions (Figure 5b). More positive E_{rep} values for Mo-3.2 than Mo-0 were observed in both environments with less variability than changes in E_{pit}, indicating that Mo may enhance repassivation (Figures 5c, 5f). Such findings suggest that Mo plays a more prominent role in pit propagation and stability than initiation. Mo enrichment suggested by decreased dissolution rates at transpassive potentials relative to bulk composition (Figure 6) may be attributable to the local decrease in pH leading to the deposition of Mo-rich corrosion products [70]. Mo has been reported to help reform a stable passive film in mild acids after surface activation caused either by the applied cathodic potential [71] or by mechanical scratching [24]. In this case, the Mo-containing passive film may serve as a catalyst for the hydrogen

Journal Pre-proof

evolution reaction [72] resulting in a high cathodic current density in this potential domain. High Mo valence within the passive film may add charge carriers which in turn support charge transfer reactions such as the oxygen evolution reaction [35]. For instance, Mo(IV)/(VI) doping in Cr(III) oxide leads to cation vacancies and/or excess free electrons [27].

Frequent pitting at the interface between FCC and $L2_1$ (Figure 8) is observed, identifying a microstructural feature responsible for pit initiation. This location suggests a role of grain boundaries or phase interfaces as possible contributors to the weakening of localized corrosion resistance, potentially due to the formation of defects in the passive film [73]. While increasing Mo concentration decreases pit initiation frequency in single-phase stainless steels and Ni-Cr-Mo alloys [74, 75], interface pitting may hinder the effect of Mo. Interfaces likely have less prominent effects on repassivation than initiation as the pit is grown well beyond the interface. The beneficial effects of Mo on pit repassivation (Figure 5) suggest Mo slows propagation or enhances repassivation unhindered by the interface. Furthermore, the increase in compositional partitioning in the alloy at higher Mo concentrations (Table II) may indicate localized depletion of passivating elements (e.g. Ti, Al) that may harm resistance to localized corrosion, particularly at or near the bulk metal phase interfaces (and resultant oxide film interfaces) where the film may be vulnerable to breakdown [21, 76]. Further evaluation with high resolution Auger electron spectroscopy of the variation in both bulk metal and passive film chemistry across the phase interface, including the position and local enrichment of Mo, will be discussed in a forthcoming publication. Adverse effects of partitioning may limit the otherwise beneficial effects of Mo. This is shown by lowering of E_{pit} distributions with increasing Mo concentration in basic environments, where Mo dissolution is likely and adverse microstructural effects may be more prominent (Figures 5b, 5e). Despite clear effects of Mo on microstructural partitioning, neither imaging of corroded surfaces (Figure 8) nor transpassive elemental dissolution rates (Table IV) suggest preferential dissolution of either phase.

Journal Pre-proof

Higher concentrations of Mo in the CCA correspond to slightly increased levels of partitioning, where the concentration of an element in the second phase differs from that in the matrix to a greater extent than in the case of CCAs with less Mo, illustrating a secondary, but still important, microstructural effect of Mo. The σ phase that has been previously shown to harm corrosion resistance with increasing Mo in CCAs [20, 41, 43] was not formed, likely due to the comparatively low concentration of both Cr and Mo. Mo is enriched in the FCC matrix phase, despite its prominent role as a ferritic stabilizer. Such lateral variation of Mo content in the passive film chemistry has been shown to promote selective dissolution in CoCrFeMoNi [77], but such behavior is not observed in the evaluated system (Figure 8).

Although Mo is not enriched in the $L2_1$ second phase, Al, Ni, and Ti generally increase in concentration in the second phase with increasing Mo concentrations (Table II). For example, the Ti content in the $L2_1$ phase of Mo-3.2 is over three times the Ti content in the matrix, whereas the Ti content in the $L2_1$ phase of Mo-0 is approximately twice that of the matrix. Similarly, Al concentrations in the $L2_1$ phase of Mo-0 are 2.5 times those of the matrix whereas the ratio between the same phases of Mo-3.2 is over four. This follows previous trends of Mo enrichment in phases differing from those enriched in Ti [41] and Al [40] in similar CCAs, with both elements possibly being driven away from the Mo-enriched FCC phase by the unfavorable enthalpies of mixing [78]. The enrichment of Ti and Al in phases depleted of Mo, rather than the FCC phase which is enriched Cr and Mo, may limit the ability for synergetic behavior in the passive film, particularly given high importance of Ti in the passivation process suggested by surface cation fractions (Figure 13, Table IX).

The beneficial contributions of Mo must be balanced with potential effects of phase partitioning of second phase-enriched elements on localized corrosion, adding a layer of complexity to previously established trends in the single-phase Fe-Cr-Mo and Ni-Cr-Mo systems. Unlike the proposed beneficial effects of low Mn concentrations on elemental degree of partitioning, poor passivation, and overall corrosion resistance observed in a similar CCA system [18], Mo concentrations must be limited to avoid

Journal Pre-proof

detrimental levels of partitioning. The addition of Mn or other FCC stabilizing elements could help increase the maximum allowable Mo content without harmful chemical segregation in the microstructure, but corrosion resistance may also be harmed by poor Mn passivation [79, 80]. Although Ni passivation is suppressed, low transpassive Ni dissolution rates (Table IV) may suggest alternative fates such as enrichment at the metal-oxide interface [54, 81].

The effect of Mo on Ni partitioning is noteworthy as the binary enthalpy of mixing between Mo and Ni is higher than that between Mo and other system elements [78]. The unfavorable interaction between Mo and Ni may preferentially cause Ni to enrich in the Mo-depleted second phase. Unlike the case of Al and Ti, increased Mo concentration does not consistently increase the degree of Ni partitioning, although the uncharacteristically low Ni composition in the FCC phase of Mo-0 highlights uncertainty in the EDS point scans. In addition to microstructural factors, increasing Mo concentrations also reduced the concentration of $Ni(OH)_2$, following trends in the Ni-Cr-Mo system proposed by Lutton et al. [32] where Ni was also less present in the passive film due to the enhancement of other passivating elements such as Cr.

Effect of Mo on Passive Film Composition

Mo is also considered with respect to its effects on global passive film chemistry. Cr is the primary passivating species in all three CCAs and in both pH values. However, the passive film concentration varies across the three alloys. Mo is not a primary passivator in any of the evaluated CCAs, although in both Mo-containing CCAs, the passive film is enriched in Mo(IV)/Mo(VI) at the film-electrolyte interface relative to bulk composition at similar ratios (Figure 13, Table IX). Notably, Mo content may be lower at film depths approaching the metal-film interface, given the tendency of Mo to enrich within outer layers of passive films formed on similar alloys [7, 27, 47, 77, 82-85]. Significant presence of Mo in the passive film is unsurprising given the thermodynamic stability of Mo oxides in a pure Mo system at pH 4 near -0.2 V_{SCE}

Journal Pre-proof

[63]. Mo(IV)/Mo(VI) cations are still suggested to be present in the passive film, although at lower concentrations in the Mo-3.2 film formed in pH 10 solution even though Mo oxides are not thermodynamically predicted to be stable. Despite low concentration in the bulk alloy, the presence of Mo in the alloy affects the passive film chemistry and possibly ionic defect status. As Mo concentration increases in the evaluated CCAs, Cr(III), Fe(II)/Fe(III), and Ni(II) content decrease while Al(III), Mo(VI), and Ti(VI) increase in the electrochemically formed passive films (Figure 13, Table IX).

Increased Mo concentration promoted Cr(III) passivation in the Ni-Cr-Mo system explored by Lutton et al. [27, 86], particularly in Cl^- environments where Ni dissolved. In contrast, the CCAs with the highest Mo concentrations have the lowest surface cation fraction of Cr in the passive film formed in the pH 4 environment despite still being enriched relative to bulk alloy composition (Figure 13, Table IX). While Ti preferentially partitions to the $L2_1$ phase, enough is still present in the FCC phase to affect global passive film chemistry. Thus, the limitation of the Cr(III) content in passive film of the CCA system may also be attributed to the high stability of Ti(IV) in the passive film. In the Ni-Cr-Mo system, Cr_2O_3 is the most stable oxide (ΔG_f° = -1050 kJ/mol) [87] whereas in the CCAs evaluated, Ti may be a preferential site for oxidation given the lower free energy of formation on a per cation basis of TiO_2 (ΔG_f° = -889 kJ/mol) [87]. Likewise, very little Al_2O_3 (ΔG_f° = -1580 kJ/mol) [87] was observed in Mo-0 while the film grown on Mo-3.2 was enriched in Al(III). Additionally, Mo-3.2 did not form any observable $Ni(OH)_2$ species in the passive film (ΔG_f° = -447 kJ/mol) [88] and had the highest combined concentration of Al(III), Cr(III), and Ti(IV) species. Thus, across both systems, Mo may be suggested to promote the presence of more stable oxide species.

Mo may affect the passive film composition by acting as an aliovalent dopant. XPS fitting (Figure 14) suggests that while oxidized Mo is dominated by Mo(VI) cations, Mo(IV) is also present. Mo(V) may have also been present given frequent observation in Ni-Cr-Mo alloys [28, 35, 86, 89], but was not identified, possibly due to overlap with other valence states. In the Ni-Cr-Mo system, Mo(IV) appears to stabilize Cr passivation while Mo(VI) cations are considered more likely to dissolve [71], however

Journal Pre-proof

conflicting results have been suggested in $CoCrFeMnNiMo_x$ CCAs [43]. The higher valence state Mo cations may be reduced to lower valence states to locally stabilize the higher valence Ti(IV) cations relative to Cr(III) and Al(III), potentially through affecting the local stability of O vacancies [90]. During the growth of the oxide in 0.1 M NaCl pH 4 (Figure 10), the current density was lowest for Mo-3.2, suggesting slower passivation kinetics along with the well-known properties of aliovalent Mo cations [27].

A significant local enrichment of Mo(0) might support Mo acting as an non-oxidized dissolution blocker [24], whereas preservation or local enrichment of the oxidized states may favor mechanisms dependent on passivated Mo [27, 30, 31, 47]. Both valence states are suggested to be present within or near the passive film by XPS (Figure 14). However, under both Mo(0)-based mechanisms, Mo depletion in the $L2_1$ phase would limit the ability of the CCAs to resist localized corrosion within the $L2_1$ phase or at the FCC-$L2_1$ interface and mechanisms dependent on Mo dissolution must also be considered. Mo dissolution occurred across of a range of potentials, most noticeably in the cathodic region due to the well-known stability of MoO_4^{2-} in alkaline solutions [63]. However, this was attributed to dissolution of the air-formed oxide, which has been shown to have high concentrations of Mo in similar CCAs [7]. Additionally, dissolution of air-formed oxides has yielded similar cathodic dissolution rates in the Ni-Cr-Mo system [71]. The likely proposed mechanism relating Mo dissolution to corrosion resistance is that MoO_4^{2-} ions act as an inhibitor to limit pit stability [23, 91], a possibility indicated by significant Mo dissolution being observed via AESEC (Figures 6, 11), especially in pH 10 solution. In this case, Mo does not have to originate in the $L2_1$ phase or near the interface, but can be supplied from the FCC phase and transported via comparatively more rapid liquid phase diffusion.

Comparative Effects of Mo under Acidic and Basic Conditions

Elemental dissolution trends measured with AESEC generally follow those predicted by the electrochemical stability of pure constituent elements for a given solution pH [63]. Pure Fe and Ni are

Journal Pre-proof

predicted to dissolve at pH 4 and form insoluble species at pH 10 [63] at -0.2 V_{SCE}. E-pH diagrams have predicted stability of both Ni oxide [63] and Ni-Cr spinel [92, 93] is more favorable under basic conditions. Therefore, XPS intensity attributable to Ni-containing complex oxide and single-cation passive species significantly increased (Figure 13, Table IX) while corresponding Ni dissolution rates decreased in basic conditions (Figure 11). Fe and Ni dissolve at pH 4 while they are below the detection limit at pH 10 at this potential for CCAs investigated in this work (Figures 11). Fe and Ni dissolve at a lower potentials than the other elements at both pH (Figure 6), and are depleted in the passive film at pH 4, as observed via XPS (Figure 13, Table IX). Despite thermodynamic instability, limited presence of Ni and Fe in the passive films formed at pH 4 indicate metastable oxide presence and/or stability enhanced by solubility with additional cations.

Mo dissolves at much higher rates in basic solutions (Figure 10), likely due to the stability of the MoO_4^{2-} ion [63]. The increased stability of Mo oxides in acids corresponds with an increase in the surface cation fractions attributable to oxidized Mo in the Mo-3.2 film grown in pH 4 relative to when grown in pH 10 solution (Figure 13, Table IX). The decreased Mo enrichment in the passive film with increasing pH follows previously established trends in 316L [94], Ni-Cr-Mo [32, 86], and the CoCrFeMoNi CCA [95]. Furthermore, Mo metal is stable at higher potentials in acids than bases [63], potentially explaining the cathodic dissolution of Mo observed in the basic environment that was not observed in the acid (Figures 6, S.3).

During potentiostatic passive film growth, the current density is highest for the Mo-free sample in pH 4 solution (Figure 10a), indicating that Mo may result in an enhanced passive film formation. Alternatively, current density shows inconsistent trends with Mo concentration in pH 10 solution (Figure 10b). Potentiostatic EIS further verifies that Mo-0 had the lowest R_P at pH 4 and that of Mo-3.2 was the lowest at pH 10 (Figure 12).

Journal Pre-proof

Increasing Mo concentration improves pitting resistance more prominently in acidic environments (Figure 5, Table III), similar to the case of the $Mo_{0.6}CoCrFe$ medium entropy alloy developed by Shuang et al. [96]. However, the improvement in corrosion resistance with decreasing pH observed is not present at a statistically significant level in the presently evaluated CCA series, potentially due to the lower Mo concentrations in the tested CCAs (0-3.2 at. %) than in $Mo_{0.6}CoCrFe$ (16.7 at. % Mo). The same effect is not observed with E_{rep}, where Mo resulted in higher R_P regardless of pH. Notably, the E_{rep} distribution of Mo-1.1 resembles that of Mo-3.2 in the pH 10 environment, which shows good repassivation behavior, and that of Mo-0 in pH 4, which shows poor repassivation behavior. This may indicate a lower Mo concentration is necessary for significant repassivation benefits in basic conditions.

Conclusions

Three $Al_{0.3}Cr_{0.5}Fe_2Mo_xNi_{1.5}Ti_{0.3}$ (x = 0, 0.05, 0.15) CCAs with Mo concentrations of 0, 1.1, and 3.2 at. % were synthesized and characterized to elucidate connections between microstructure and corrosion resistance with the main motivation to investigate the benefits of Mo in Cr-lean CCAs containing Al and Ti as passivators. The following conclusions were obtained:

- An FCC matrix enriched in Fe, Cr, and Mo (when added as alloying element) with $L2_1$ regions enriched in Al, Ti, and Ni was present for all CCAs. Mo is found to have indirect effects on corrosion through its impact on elemental partitioning after heat treatment at 1070 ˚C. The microstructural partitioning affects the nature of films grown on CCAs with increased Mo concentration, particularly with regards to the concentration of elements that preferentially partition to the second phase such as Ti. Such changes in element partitioning are shown to alter passive film chemistry, and thus have a significant effect on the corrosion behavior that must be accounted for within the alloy design process.

Journal Pre-proof

- The resistance to localized corrosion was improved with increased Mo concentration both during potentiodynamic polarization and long-term immersion, most noticeably through improvements in the repassivation potential. Pitting often occurred at the FCC-$L2_1$ interfaces, particularly in low-Mo CCAs, but neither phase was vulnerable to selective dissolution.
- Mo also affects passivity and passive film chemistry. Decreased passive current densities and more positive repassivation potential with Mo content may suggest Mo slows corrosion reaction kinetics through solid state effects in the passive film. Species found in the passive films of CCAs with higher Mo concentration generally had more negative standard free energies, and did not appear to be limited in passivation by local enrichments in the microstructure. The overall corrosion resistance was generally worse than 316L in both acidic and basic environments, which may be attributable to the lean Cr contents compared to the high Cr content 316L as well as the microstructure containing two phases with corresponding interfaces.
- Trends in corrosion behavior with Mo content are less prominent in Al and Ti containing CCAs than single-phase alloy dependent on only Cr for passivity. The CCA design space introduces a variety of effects of alloying elements such as Mo with both metallurgical and passivity roles that have secondary effects on passivation that are not observed in single-phase or less complex alloys.

Journal Pre-proof

Acknowledgements

This work was supported by the United States Office of Naval Research under grant # N00014-19-1-2420. Use of the Empyrean™ Diffractometer, Quanta 650™ SEM, and PHI VersaProbe III™ XPS was made possible by the University of Virginia Nanomaterials Characterization Facility. The PHI VersaProbe III was procured under NSF award # 162601. Author K. Ogle and the AESEC equipment were supported by Agence Nationale de Recherche, award # ANR-20-CE08-0031 (TAPAS 2020). Kaitlyn Anderson contributed

to the electrochemical characterization. S. Joseph Poon contributed to funding acquisition and sample synthesis.

References[97]

[1] D.B. Miracle, O.N. Senkov, A critical review of high entropy alloys and related concepts, Acta Materialia, 122 (2017) 448-511.
[2] Y. Qiu, S. Thomas, M.A. Gibson, H.L. Fraser, N. Birbilis, Corrosion of high entropy alloys, npj Materials Degradation, 1 (2017) 15.
[3] J.R. Scully, S.B. Inman, A.Y. Gerard, C.D. Taylor, W. Windl, D.K. Schreiber, P. Lu, J.E. Saal, G.S. Frankel, Controlling the corrosion resistance of multi-principal element alloys, Scripta Materialia, 188 (2020) 96-101.
[4] M.-H. Tsai, J.-W. Yeh, High-Entropy Alloys: A Critical Review, Materials Research Letters, 2 (2014) 107-123.
[5] E.P. George, D. Raabe, R.O. Ritchie, High-entropy alloys, Nature Reviews Materials, 4 (2019) 515-534.
[6] R. Feng, C. Lee, M. Mathes, T.T. Zuo, S. Chen, J. Hawk, Y. Zhang, P. Liaw, Design of Light-Weight High-Entropy Alloys, Entropy, 18 (2016) 333.
[7] S.B. Inman, D. Sur, J. Han, K. Ogle, J.R. Scully, Corrosion Behavior of a Compositionally Complex Alloy Utilizing Simultaneous Al, Cr, and Ti Passivation, Corroison Science, 217 (2023) 111138.
[8] Y. Qiu, R. Liu, T. Gengenbach, O. Gharbi, S. Choudhary, S. Thomas, H.L. Fraser, N. Birbilis, Real-time dissolution of a compositionally complex alloy using inline ICP and correlation with XPS, npj Materials Degradation, 4 (2020) 7.
[9] C.P. Lee, C.C. Chang, Y.Y. Chen, J.W. Yeh, H.C. Shih, Effect of the aluminium content of AlxCrFe1.5MnNi0.5 high-entropy alloys on the corrosion behaviour in aqueous environments, Corrosion Science, 50 (2008) 2053-2060.
[10] B.-y. Li, K. Peng, A.-p. Hu, L.-p. Zhou, J.-j. Zhu, D.-y. Li, Structure and properties of FeCoNiCrCu0.5Alx high-entropy alloy, Transactions of Nonferrous Metals Society of China, 23 (2013) 735-741.
[11] Y. Qiu, S. Thomas, D. Fabijanic, A.J. Barlow, H.L. Fraser, N. Birbilis, Microstructural evolution, electrochemical and corrosion properties of AlxCoCrFeNiTiy high entropy alloys, Materials & Design, 170 (2019) 107698.
[12] Z. Tang, L. Huang, W. He, P. Liaw, Alloying and Processing Effects on the Aqueous Corrosion Behavior of High-Entropy Alloys, Entropy, 16 (2014) 895-911.
[13] D.H. Xiao, P.F. Zhou, W.Q. Wu, H.Y. Diao, M.C. Gao, M. Song, P.K. Liaw, Microstructure, mechanical and corrosion behaviors of AlCoCuFeNi-(Cr,Ti) high entropy alloys, Materials & Design, 116 (2017) 438-447.
[14] D. Yang, Y. Liu, H. Jiang, M. Liao, N. Qu, T. Han, Z. Lai, J. Zhu, A novel FeCrNiAlTi-based high entropy alloy strengthened by refined grains, Journal of Alloys and Compounds, 823 (2020) 153729.
[15] W. Guo, J. Li, M. Qi, Y. Xu, H.R. Ezatpour, Effects of heat treatment on the microstructure, mechanical properties and corrosion resistance of AlCoCrFeNiTi0.5 high-entropy alloy, Journal of Alloys and Compounds, 884 (2021) 161026.

Journal Pre-proof

[16] Y. Shi, L. Collins, R. Feng, C. Zhang, N. Balke, P.K. Liaw, B. Yang, Homogenization of AlxCoCrFeNi high-entropy alloys with improved corrosion resistance, Corrosion Science, 133 (2018) 120-131.
[17] D. Choudhuri, T. Alam, T. Borkar, B. Gwalani, A.S. Mantri, S.G. Srinivasan, M.A. Gibson, R. Banerjee, Formation of a Huesler-like L21 phase in a CoCrCuFeNiAlTi high-entropy alloy, Scripta Materialia, 100 (2015) 36-39.
[18] S.B. Inman, J. Han, A.Y. Gerard, J. Qi, M.A. Wischhusen, S.R. Agnew, S.J. Poon, K. Ogle, J.R. Scully, Effect of Mn Content on the Passivation and Corrosion of Al0.3Cr0.5Fe2MnxMo0.15Ni1.5Ti0.3 Compositionally Complex Face-Centered Cubic Alloys, Corrosion, 78 (2021) 32-48.
[19] K. Ishikawa, I. Ohnuma, R. Kainuma, K. Aoki, K. Ishida, Phase equilibria and stability of Heusler-type aluminides in the NiAl–Ni2AlTi–Ni2AlY (Y: V, Cr or Mn) systems, Journal of Alloys and Compounds, 367 (2004) 2-9.
[20] W. Wang, J. Wang, H. Yi, W. Qi, Q. Peng, Effect of Molybdenum Additives on Corrosion Behavior of (CoCrFeNi)(100-x)Mo(x) High-Entropy Alloys, Entropy (Basel), 20 (2018) 908.
[21] Y. Shi, L. Collins, N. Balke, P.K. Liaw, B. Yang, In-situ electrochemical-AFM study of localized corrosion of AlxCoCrFeNi high-entropy alloys in chloride solution, Applied Surface Science, 439 (2018) 533-544.
[22] M. Klimmeck, A study of the kinetics of passive layer formation on Cr-Mo alloys, Electrochimica Acta, 25 (1980) 1375-1381.
[23] K. Sugimoto, Y. Sawada, The role of molybdenum additions to austenitic stainless steels in the inhibition of pitting in acid chloride solutions, Corrosion Science, 17 (1977) 425-445.
[24] R.C. Newman, The dissolution and passivation kinetics of stainless alloys containing molybdenum—1. Coulometric studies of Fe-Cr and Fe-Cr-Mo alloys, Corrosion Science, 25 (1985) 331-339.
[25] K. Hashimoto, K. Asami, K. Teramoto, An X-ray photo-electron spectroscopic study on the role of molybdenum in increasing the corrosion resistance of ferritic stainless steels in HC1, Corrosion Science, 19 (1979) 3-14.
[26] Y. Shi, B. Yang, P.K. Liaw, Corrosion-Resistant High-Entropy Alloys: A Review, Metals, 7 (2017) 43.
[27] K. Lutton Cwalina, C.R. Demarest, A.Y. Gerard, J.R. Scully, Revisiting the effects of molybdenum and tungsten alloying on corrosion behavior of nickel-chromium alloys in aqueous corrosion, Current Opinion in Solid State and Materials Science, 23 (2019) 129-141.
[28] N. Ebrahimi, M.C. Biesinger, D.W. Shoesmith, J.J. Noël, The influence of chromium and molybdenum on the repassivation of nickel-chromium-molybdenum alloys in saline solutions, Surface and Interface Analysis, 49 (2017) 1359-1365.
[29] P.I. Marshall, G.T. Burstein, Effects of alloyed molybdenum on the kinetics of repassivation on austenitic stainless steels, Corrosion Science, 24 (1984) 463-478.
[30] J.D. Henderson, X. Li, F.P. Filice, D. Zagidulin, M.C. Biesinger, B. Kobe, D.W. Shoesmith, K. Ogle, J.J. Noël, Investigating the Role of Mo and Cr during the Activation and Passivation of Ni-Based Alloys in Acidic Chloride Solution, Journal of The Electrochemical Society, 168 (2021) 021509.
[31] G. Tranchida, F. Di Franco, M. Santamaria, Role of Molybdenum on the Electronic Properties of Passive Films on Stainless Steels, Journal of The Electrochemical Society, 167 (2020) 061506.
[32] K.L. Cwalina, H.M. Ha, N. Ott, P. Reinke, N. Birbilis, J.R. Scully, In Operando Analysis of Passive Film Growth on Ni-Cr and Ni-Cr-Mo Alloys in Chloride Solutions, Journal of The Electrochemical Society, 166 (2019) C3241-C3253.
[33] A.C. Lloyd, J.J. Noël, S. McIntyre, D.W. Shoesmith, Cr, Mo and W alloying additions in Ni and their effect on passivity, Electrochimica Acta, 49 (2004) 3015-3027.
[34] K. Gusieva, K.L. Cwalina, W.H. Blades, G. Ramalingam, J.H. Perepezko, P. Reinke, J.R. Scully, Repassivation Behavior of Individual Grain Facets on Dilute Ni–Cr and Ni–Cr–Mo Alloys in Acidified Chloride Solution, The Journal of Physical Chemistry C, 122 (2018) 19499-19513.

Journal Pre-proof

[35] A. Larsson, A. Grespi, G. Abbondanza, J. Eidhagen, D. Gajdek, K. Simonov, X. Yue, U. Lienert, Z. Hegedüs, A. Jeromin, T.F. Keller, M. Scardamaglia, A. Shavorskiy, L.R. Merte, J. Pan, E. Lundgren, The Oxygen Evolution Reaction Drives Passivity Breakdown for Ni–Cr–Mo Alloys, Advanced Materials, 35 (2023) 2304621.
[36] D.A. Stout, J.B. Lumsden, R.W. Staehle, An Investigation of Pitting Behavior of Iron-Molybdenum Binary Alloys, Corrosion, 35 (1979) 141-147.
[37] X. Wang, D. Mercier, S. Zanna, A. Seyeux, L. Perriere, M. Laurent-Brocq, I. Guillot, V. Maurice, P. Marcus, Effects of Chloride Ions on Passive Oxide Films Formed on Cr-Fe-Co-Ni(-Mo) Multi-Principal Element Alloy Surfaces, Journal of The Electrochemical Society, 170 (2023) 041506.
[38] Y. Liu, Y. Xie, S. Cui, Y. Yi, X. Xing, X. Wang, W. Li, Effect of Mo Element on the Mechanical Properties and Tribological Responses of CoCrFeNiMox High-Entropy Alloys, Metals, 11 (2021) 486.
[39] C. Dai, Y. Fu, Y. Pan, Y. Yin, C. Du, Z. Liu, Microstructure and mechanical properties of FeCoCrNiMo0.1 high-entropy alloy with various annealing treatments, Materials Characterization, 179 (2021) 111313.
[40] J.M. Zhu, H.M. Fu, H.F. Zhang, A.M. Wang, H. Li, Z.Q. Hu, Microstructures and compressive properties of multicomponent AlCoCrFeNiMox alloys, Materials Science and Engineering: A, 527 (2010) 6975-6979.
[41] Y.L. Chou, J.W. Yeh, H.C. Shih, The effect of molybdenum on the corrosion behaviour of the high-entropy alloys Co1.5CrFeNi1.5Ti0.5Mox in aqueous environments, Corrosion Science, 52 (2010) 2571-2581.
[42] A.A. Rodriguez, J.H. Tylczak, M.C. Gao, P.D. Jablonski, M. Detrois, M. Ziomek-Moroz, J.A. Hawk, Effect of Molybdenum on the Corrosion Behavior of High-Entropy Alloys CoCrFeNi2 and CoCrFeNi2Mo0.25 under Sodium Chloride Aqueous Conditions, Advances in Materials Science and Engineering, 2018 (2018) 3016304.
[43] X.-L. Shang, W. Zhijun, Q.-F. Wu, J.-C. Wang, J.-J. Li, J.-K. Yu, Effect of Mo Addition on Corrosion Behavior of High-Entropy Alloys CoCrFeNiMox in Aqueous Environments, Acta Metallurgica Sinica (English Letters), 32 (2018).
[44] C. Ren, K. Sun, Y.F. Jia, N.Z. Zhang, Y.D. Jia, G. Wang, Effect of Mo addition on the microstructural evolution and mechanical properties of Fe–Ni–Cr–Mn–Al–Ti high entropy alloys, Materials Science and Engineering: A, 864 (2023) 144579.
[45] Linder, Clara and Rao, Smita G. and Boyd, Robert and Greczynski, Grzegorz and Eklund, Per and Munktell, Sara and le Febvrier, Arnaud and Björk, Emma M., Effect of Mo Content on the Corrosion Resistance of CoCrFeMoxNi Thin Films in Sulfuric Acid. Available at SSRN: https://ssrn.com/abstract=4481216 or http://dx.doi.org/10.2139/ssrn.4481216.
[46] Z. Niu, Y. Wang, C. Geng, J. Xu, Y. Wang, Microstructural evolution, mechanical and corrosion behaviors of as-annealed CoCrFeNiMox (x = 0, 0.2, 0.5, 0.8, 1) high entropy alloys, Journal of Alloys and Compounds, 820 (2020) 153273.
[47] X. Wang, D. Mercier, S. Zanna, A. Seyeux, L. Perriere, M. Laurent-Brocq, I. Guillot, V. Maurice, P. Marcus, Origin of enhanced passivity of Cr–Fe–Co–Ni–Mo multi-principal element alloy surfaces, npj Materials Degradation, 7 (2023) 13.
[48] B. Cantor, I.T.H. Chang, P. Knight, A.J.B. Vincent, Microstructural development in equiatomic multicomponent alloys, Materials Science and Engineering: A, 375-377 (2004) 213-218.
[49] C. Sun, R. Xiao, H. Li, Y. Ruan, Effects of phase selection and microsegregation on corrosion behaviors of Ti-Al-Mo alloys, Corrosion Science, 200 (2022) 110232.
[50] Y. Shi, B. Yang, X. Xie, J. Brechtl, K.A. Dahmen, P.K. Liaw, Corrosion of Al xCoCrFeNi high-entropy alloys: Al-content and potential scan-rate dependent pitting behavior, Corrosion Science, 119 (2017) 33-45.

Journal Pre-proof

[51] J.J. Bhattacharyya, S.B. Inman, M.A. Wischhusen, J. Qi, J. Poon, J.R. Scully, S.R. Agnew, Lightweight, Low Cost Compositionally Complex Multiphase Alloys with Optimized Strength, Ductility and Corrosion Resistance: Discovery, Design and Mechanistic Understandings, Submitted to Materials and Design, (2023).
[52] C.O.A. Olsson, D. Landolt, Passive films on stainless steels—chemistry, structure and growth, Electrochimica Acta, 48 (2003) 1093-1104.
[53] J. Qi, A.M. Cheung, S.J. Poon, High Entropy Alloys Mined From Binary Phase Diagrams, Scientific Reports, 9 (2019) 15501.
[54] A.Y. Gerard, J. Han, S.J. McDonnell, K. Ogle, E.J. Kautz, D.K. Schreiber, P. Lu, J.E. Saal, G.S. Frankel, J.R. Scully, Aqueous passivation of multi-principal element alloy Ni38Fe20Cr22Mn10Co10: Unexpected high Cr enrichment within the passive film, Acta Materialia, 198 (2020) 121-133.
[55] ASTM, Standard Guide for Applying Statistics to Analysis of Corrosion Data, in, 2010.
[56] B.A. Kehler, G.O. Ilevbare, J.R. Scully, Crevice Corrosion Stabilization and Repassivation Behavior of Alloy 625 and Alloy 22, Corrosion, 57 (2001) 1042-1065.
[57] B.A. Kehler, J.R. Scully, Role of Metastable Pitting in Crevices on Crevice Corrosion Stabilization in Alloys 625 and 22, Corrosion, 61 (2005) 665-684.
[58] K. Ogle, Atomic Emission Spectroelectrochemistry: Real-Time Rate Measurements of Dissolution, Corrosion, and Passivation, Corrosion, 75 (2019) 1398-1419.
[59] M.C. Biesinger, B.P. Payne, A.P. Grosvenor, L.W.M. Lau, A.R. Gerson, R.S.C. Smart, Resolving surface chemical states in XPS analysis of first row transition metals, oxides and hydroxides: Cr, Mn, Fe, Co and Ni, Applied Surface Science, 257 (2011) 2717-2730.
[60] M.C. Biesinger, L.W.M. Lau, A.R. Gerson, R.S.C. Smart, Resolving surface chemical states in XPS analysis of first row transition metals, oxides and hydroxides: Sc, Ti, V, Cu and Zn, Applied Surface Science, 257 (2010) 887-898.
[61] J. Baltrusaitis, B. Mendoza-Sanchez, V. Fernandez, R. Veenstra, N. Dukstiene, A. Roberts, N. Fairley, Generalized molybdenum oxide surface chemical state XPS determination via informed amorphous sample model, Applied Surface Science, 326 (2015) 151-161.
[62] A. Obrosov, R. Gulyaev, A. Zak, M. Ratzke, M. Naveed, W. Dudzinski, S. Weiß, Chemical and Morphological Characterization of Magnetron Sputtered at Different Bias Voltages Cr-Al-C Coatings, in: Materials, 2017.
[63] M. Pourbaix, Atlas of electrochemical equilibria in aqueous solutions, (1974).
[64] B. Hirschorn, M.E. Orazem, B. Tribollet, V. Vivier, I. Frateur, M. Musiani, Constant-Phase-Element Behavior Caused by Resistivity Distributions in Films: I. Theory, Journal of The Electrochemical Society, 157 (2010) C452.
[65] H.H. Uhlig, G.E. Woodside, Anodic Polarization of Passive and Non-passive Chromium–Iron Alloys, The Journal of Physical Chemistry, 57 (1953) 280-283.
[66] H.H. Uhlig, Electron configuration in alloys and passivity, Zeitschrift für Elektrochemie, Berichte der Bunsengesellschaft für physikalische Chemie, 62 (1958) 700-707.
[67] J. Peng, F. Moszner, J. Rechmann, D. Vogel, M. Palm, M. Rohwerder, Influence of Al content and pre-oxidation on the aqueous corrosion resistance of binary Fe-Al alloys in sulphuric acid, Corrosion Science, 149 (2019) 123-132.
[68] A.S. Lim, A. Atrens, ESCA studies of Fe-Ti alloys, Applied Physics A, 54 (1992) 500-507.
[69] W.H. Blades, B.W.Y. Redemann, N. Smith, D. Sur, M.S. Barbieri, Y. Xie, S. Lech, E. Anber, M.L. Teheri, C. Wolverton, T.M. McQueen, J.R. Scully, K. Seradzki, Tuning Chemical Short-range Order for Stainless Behavior at Reduced Chromium Concentrations in Multi-principal Element Alloys, Submitted to Nature Materials, (2023).
[70] J.D. Henderson, X. Li, D.W. Shoesmith, J.J. Noël, K. Ogle, Molybdenum surface enrichment and release during transpassive dissolution of Ni-based alloys, Corrosion Science, 147 (2019) 32-40.

Journal Pre-proof

[71] X. Li, J.D. Henderson, F.P. Filice, D. Zagidulin, M.C. Biesinger, F. Sun, B. Qian, D.W. Shoesmith, J.J. Noël, K. Ogle, The contribution of Cr and Mo to the passivation of Ni22Cr and Ni22Cr10Mo alloys in sulfuric acid, Corrosion Science, 176 (2020) 109015.
[72] S.H. Park, D.T. To, N.V. Myung, A review of nickel-molybdenum based hydrogen evolution electrocatalysts from theory to experiment, Applied Catalysis A: General, 651 (2023) 119013.
[73] P. Marcus, V. Maurice, Atomic level characterization in corrosion studies, Philosophical Transactions of the Royal Society A: Mathematical, Physical and Engineering Sciences, 375 (2017) 20160414.
[74] G.O. Ilevbare, G.T. Burstein, The role of alloyed molybdenum in the inhibition of pitting corrosion in stainless steels, Corrosion Science, 43 (2001) 485-513.
[75] B.A. Kehler, J. Scully, Role of Metastable Pitting in Crevices on Crevice Corrosion Stabilizationin Alloys 625 and 22, Corrosion, 61 (2005).
[76] P. Marcus, V. Maurice, H.H. Strehblow, Localized corrosion (pitting): A model of passivity breakdown including the role of the oxide layer nanostructure, Corrosion Science, 50 (2008) 2698-2704.
[77] Z. Wang, Z.-X. Liu, J. Jin, D.-Z. Tang, L. Zhang, Selective corrosion mechanism of CoCrFeMoNi high-entropy alloy in the transpassive region based on the passive film characterization by ToF-SIMS, Corrosion Science, 218 (2023) 111206.
[78] A. Takeuchi, A. Inoue, Classification of Bulk Metallic Glasses by Atomic Size Difference, Heat of Mixing and Period of Constituent Elements and Its Application to Characterization of the Main Alloying Element, Materials Transactions, 46 (2005) 2817-2829.
[79] H. Torbati-Sarraf, M. Shabani, P.D. Jablonski, G.J. Pataky, A. Poursaee, The influence of incorporation of Mn on the pitting corrosion performance of CrFeCoNi High Entropy Alloy at different temperatures, Materials & Design, 184 (2019) 108170.
[80] J. Yang, J. Wu, C.Y. Zhang, S.D. Zhang, B.J. Yang, W. Emori, J.Q. Wang, Effects of Mn on the electrochemical corrosion and passivation behavior of CoFeNiMnCr high-entropy alloy system in H2SO4 solution, Journal of Alloys and Compounds, 819 (2020) 152943.
[81] L. Wang, D. Mercier, S. Zanna, A. Seyeux, M. Laurent-Brocq, L. Perrière, I. Guillot, P. Marcus, Study of the surface oxides and corrosion behaviour of an equiatomic CoCrFeMnNi high entropy alloy by XPS and ToF-SIMS, Corrosion Science, 167 (2020) 108507.
[82] K.F. Quiambao, S.J. McDonnell, D.K. Schreiber, A.Y. Gerard, K.M. Freedy, P. Lu, J.E. Saal, G.S. Frankel, J.R. Scully, Passivation of a corrosion resistant high entropy alloy in non-oxidizing sulfate solutions, Acta Materialia, 164 (2019) 362-376.
[83] B. Lynch, Z. Wang, L. Ma, E.-M. Paschalidou, F. Wiame, V. Maurice, P. Marcus, Passivation-Induced Cr and Mo Enrichments of 316L Stainless Steel Surfaces and Effects of Controlled Pre-Oxidation, Journal of The Electrochemical Society, 167 (2020) 141509.
[84] Z. Wang, E.-M. Paschalidou, A. Seyeux, S. Zanna, V. Maurice, P. Marcus, Mechanisms of Cr and Mo Enrichments in the Passive Oxide Film on 316L Austenitic Stainless Steel, Frontiers in Materials, 6 (2019).
[85] J. Eidhagen, A. Larsson, A. Preobrajenski, A. Delblanc, E. Lundgren, J. Pan, Synchrotron XPS and Electrochemical Study of Aging Effect on Passive Film of Ni Alloys, Journal of The Electrochemical Society, 170 (2023) 021506.
[86] K. Lutton, J. Han, H.M. Ha, D. Sur, E. Romanovskaia, J.R. Scully, Passivation of Ni-Cr and Ni-Cr-Mo Alloys in Low and High pH Sulfate Solutions, Journal of The Electrochemical Society, 170 (2023) 021507.
[87] M.W. Chase, JANAF Thermochemical Tables, 4th Edition, Journal of Physical and Chemical Reference Data, in: NIST (Ed.), 1998.
[88] D.G. Archer, Thermodynamic Properties of Import to Environmental Processes and Remediation. II. Previous Thermodynamic Property Values for Nickel and Some of its Compounds, Journal of Physical and Chemical Reference Data, 28 (1999) 1485-1507.

Journal Pre-proof

[89] A. Larsson, G. D'Acunto, M. Vorobyova, G. Abbondanza, U. Lienert, Z. Hegedüs, A. Preobrajenski, L.R. Merte, J. Eidhagen, A. Delblanc, J. Pan, E. Lundgren, Thickness and composition of native oxides and near-surface regions of Ni superalloys, Journal of Alloys and Compounds, 895 (2022) 162657.
[90] V. Kumaravel, S. Rhatigan, S. Mathew, M.C. Michel, J. Bartlett, M. Nolan, S.J. Hinder, A. Gascó, C. Ruiz-Palomar, D. Hermosilla, S.C. Pillai, Mo doped TiO2: impact on oxygen vacancies, anatase phase stability and photocatalytic activity, Journal of Physics: Materials, 3 (2020) 025008.
[91] R.S. Lillard, M.P. Jurinski, J.R. Scully, Crevice Corrosion of Alloy 625 in Chlorinated ASTM Artificial Ocean Water, Corrosion, 50 (1994) 251-265.
[92] P. Lu, J.E. Saal, G.B. Olson, T. Li, O.J. Swanson, G.S. Frankel, A.Y. Gerard, K.F. Quiambao, J.R. Scully, Computational materials design of a corrosion resistant high entropy alloy for harsh environments, Scripta Materialia, 153 (2018) 19-22.
[93] K. Wang, J. Han, A.Y. Gerard, J.R. Scully, B.-C. Zhou, Potential-pH diagrams considering complex oxide solution phases for understanding aqueous corrosion of multi-principal element alloys, npj Materials Degradation, 4 (2020) 35.
[94] Z. Wang, Z.-Q. Zhou, L. Zhang, J.-Y. Hu, Z.-R. Zhang, M.-X. Lu, Effect of pH on the Electrochemical Behaviour and Passive Film Composition of 316L Stainless Steel, Acta Metallurgica Sinica (English Letters), 32 (2019) 585-598.
[95] Z. Wang, G.-H. Zhang, X.-H. Fan, J. Jin, L. Zhang, Y.-X. Du, Corrosion behavior and surface characterization of an equiatomic CoCrFeMoNi high-entropy alloy under various pH conditions, Journal of Alloys and Compounds, 900 (2022) 163432.
[96] S. Shuang, G.J. Lyu, D. Chung, X.Z. Wang, X. Gao, H.H. Mao, W.P. Li, Q.F. He, B.S. Guo, X.Y. Zhong, Y.J. Wang, Y. Yang, Unusually high corrosion resistance in MoxCrNiCo medium entropy alloy enhanced by acidity in aqueous solution, Journal of Materials Science & Technology, (2022).
[97] J.F. Kielkopf, New approximation to the Voigt function with applications to spectral-line profile analysis, J. Opt. Soc. Am., 63 (1973) 987-995.

Journal Pre-proof

CRediT authorship contribution statement

Samuel B. Inman: Formal analysis, Investigation, Writing - Original Draft, Visualization. Writing - Review & Editing. **Junsoo Han:** Investigation, Writing - Review & Editing. **Mark A. Wischhusen:** Investigation, Writing - Review & Editing. **Jie Qi:** Investigation, Writing - Review & Editing. **Sean R. Agnew:** Writing - Review & Editing, Supervision, Funding acquisition. **Kevin Ogle:** Methodology, Writing - Review & Editing, Supervision, Funding acquisition. **John R. Scully:** Conceptualization, Methodology, Writing - Review & Editing, Supervision, Project administration, Funding acquisition.

Declaration of interests

☒ The authors declare that they have no known competing financial interests or personal relationships that could have appeared to influence the work reported in this paper.

☐ The authors declare the following financial interests/personal relationships which may be considered as potential competing interests:

Highlights

- The passivation behavior and corrosion resistance in chloride and sulfate of a dual-phase compositionally complex alloy series with varying Mo content is characterized.
- Pitting and repassivation potentials increase with Mo concentration in acidic solutions where Mo is stable, indicating improved resistance to resistance to localized corrosion that often occurs at phase interfaces.
- Elemental fates are tracked with X-ray Photoelectron Spectroscopy and Atomic Emission Spectroelectrochemistry.
- Mo concentration affects the passive film chemistry, with Ni passivation suppressed in favor of more stable species such as TiO_2.
- The addition of Mo increases the degree of elemental partition within the FCC+$L2_1$ microstructure, potentially limiting interaction between Al, Cr, Ti, and/or Mo in the passive film.

Journal Pre-proof